

**CORROSION PROTECTION PERFORMANCE OF CATHODICALLY  
PROTECTED OIL AND GAS PIPELINE COATINGS AROUND THE  
TRANSITION TEMPERATURE**

by

**Ibrahem Abushwashi**

B.Sc. Electrical Engineering, Tripoli University, Tripoli, Libya, 1997

A THESIS SUBMITTED IN PARTIAL FULFILLMENT OF  
THE REQUIREMENTS FOR THE DEGREE OF

MASTER OF APPLIED SCIENCE

in

The Faculty of Graduate Studies

(Materials Engineering)

THE UNIVERSITY OF BRITISH COLUMBIA

(Vancouver)

April, 2014

©Ibrahem Abushwashi

## Abstract

Oil and gas pipelines are susceptible to corrosion by reacting with their environments. Water, oxidants, acids, and alkalis can act aggressively on the steel substrate. Over the years, corrosion has been the cause of many catastrophes. Thus, to prevent or slow down corrosion from taking place on steel substrate two techniques are primarily used. These techniques are coatings and cathodic protection. While the principles of cathodic protection is basically to reduce corrosion potential, coatings protect metals by breaking corrosion cells and provide shielding from corrosive agents. However, coatings should exhibit certain characteristics in order to be considered effective in terms of corrosion protection. Coatings have to withstand severe weather including temperature changes. Pipelines often operate at high temperatures due to the heat generated from crude frictions during transfer. With higher demands for crude oil and products, pipelines might be operated at flow rates more than normal and temperatures may exceed transition temperature ( $T_g$ ) of the coatings.

All thermoplastic materials have an important material property resulting from the molecular movement of the side chains of the polymer,  $T_g$ . It affects many polymer properties. In literature, it is not quite clear whether  $T_g$  affects corrosion protection properties or not. In this work, behavior of two polymer coatings, namely SP8888 and SP2888 provided by Specialty Polymer Coatings Inc., have been studied at temperatures around their  $T_g$  using Electrochemical Impedance Microscopy (EIS) in combination with Electrochemical Noise (EN). From the experimental work results, it was found that coating capacitance ( $C_c$ ) has slightly increased and coating resistance ( $R_c$ ) has decreased as temperature was increased over the range of test. There was a slope change for both  $R_c$  and  $C_c$  around  $T_g$ . Charge transfer resistance ( $R_{ct}$ ) has shown an abrupt drop as the temperature approached  $T_g$ . Generally, the estimated  $T_g$  value from  $Z$  modulus was in good compatibility with the  $T_g$  measured with other DSC technique.

## **Preface**

All the research work presented in this thesis was performed in the corrosion laboratory in the Department of Materials Engineering, University of British Columbia, under the supervision of Professor Akram Alfantazi who had provided me with suggestions for revision and had helped with all the aspects of the research work.

# Table of Contents

|  |     |
|--|-----|
| Abstract .....   | ii  |
| Preface .....  | iii |
| Table of Contents .....                                  | iv  |
| List of Tables .....                                     | vi  |
| List of Figures .....                                    | vii |
| Acknowledgment .....                                     | ix  |
| Dedication .....   | x   |
| 1 Chapter 1: Introduction .....                          | 1   |
| 2 Chapter 2: Literature review .....                     | 3   |
| 2.1 Corrosion in metals .....                            | 3   |
| 2.1.1 Electrochemistry of corrosion .....                | 3   |
| 2.1.2 Thermodynamics of corrosion .....                  | 8   |
| 2.1.3 Kinetics of corrosion .....                        | 12  |
| 2.2 Corrosion protection .....                           | 14  |
| 2.2.1 Coatings .....                                     | 14  |
| 2.2.2 Cathodic protection .....                          | 15  |
| 2.3 Polymer coatings .....                               | 16  |
| 2.3.1 Barrier property .....                             | 17  |
| 2.3.2 Sorption .....                                     | 18  |
| 2.3.3 Adhesion .....                                     | 22  |
| 2.3.4 Glass transit temperature .....                    | 24  |
| 2.4 Role of temperature .....                            | 26  |
| 2.4.1 Barrier property .....                             | 26  |
| 2.4.2 Sorption .....                                     | 29  |
| 2.4.3 Adhesion .....                                     | 31  |
| 2.5 Testing Methods .....                                | 32  |
| 2.5.1 Electrochemical impedance spectroscopy (EIS) ..... | 32  |
| 2.5.2 Electrochemical Noise .....                        | 35  |

|       |  |    |
|-------|--|----|
| 2.5.3 | Direct current resistance.....   | 40 |
| 2.5.4 | Gravimetric water uptake.....  | 40 |
| 3     | Chapter 3: Scope and objectives .....  | 42 |
| 4     | Chapter 4: Testing Materials and Experimental work .....                           | 43 |
| 4.1   | Tested materials .....   | 43 |
| 4.1.1 | Testing cell.....  | 43 |
| 4.1.2 | Electrolyte .....  | 45 |
| 4.1.3 | Faraday cage .....   | 45 |
| 4.2   | Characterization .....   | 45 |
| 4.2.1 | Differential Scanning Calorimetry (DSC) .....                                      | 45 |
| 4.2.2 | Energy-dispersive X-ray spectroscopy/ Scanning electron microscope (EDX/SEM) ..... | 46 |
| 4.2.3 | Gravimetric testing.....   | 46 |
| 4.3   | Electrochemical testing.....   | 46 |
| 4.3.1 | Electrochemical impedance spectroscopy tests (EIS).....                            | 46 |
| 4.3.2 | Electrochemical Noise tests (EN) .....   | 47 |
| 5     | Chapter 5: Results and Discussion.....   | 48 |
| 5.1   | Coating characterization .....   | 48 |
| 5.1.1 | Differential scanning calorimetry (DSC) .....                                      | 48 |
| 5.1.2 | Morphologies .....   | 50 |
| 5.1.3 | Gravimetric test.....  | 53 |
| 5.2   | Electrochemical testing .....  | 54 |
| 5.2.1 | Electrochemical Impedance Spectroscopy (EIS) .....                                 | 54 |
| 5.2.2 | Electrochemical Noise Testing (EN) .....   | 67 |
| 6     | Summary and Conclusions.....   | 71 |
| 7     | Future work.....   | 73 |
| 8     | References.....  | 74 |

## List of Tables

|  |    |
|--|----|
| Table 2-2: Water Diffusion Coefficients and sorption profile for epoxy resins (Philippe <i>et al.</i> , 2004)..... | 29 |
| Table 5-1: $T_g$ from Heat flow and non-reversing heat flow .....  | 50 |
| Table 5-2: Calculated EEC elements' values for SP2888 at different temperatures .....                              | 62 |
| Table 5-3: calculated EEC element values for SP8888 at different temperatures .....                                | 62 |
| Table 5-4: $R_n$ ( $\Omega$ )for SP2888 at temperature range of 20 to 80°C.....                                    | 68 |
| Table 5-5: $R_n$ for SP8888 at temperature range of 20 to 90°C .....   | 68 |

## List of Figures

|   |    |
|---|----|
| Figure 2-1: Salt concentration cell redrawn from (Ibrahim, 2005).....   | 5  |
| Figure 2-2: Buried pipeline exhibiting differential aeration cell. redrawn from (Ahmad, 2006a).....   | 6  |
| Figure 2-3: Pourbaix diagram for Iron at $10^{-6}$ m at 25°C (Beverkog and Puigdomenech, 1996).....   | 11 |
| Figure 2-4: Schematic of Evans diagram for Hydrogen evolution on Iron (Macdonald and Barsoukov, 2005).....  | 13 |
| Figure 2-5: $R_n$ , $Z$ and $R_{DC}$ at 3% wt NaCl for FBE coating Vs $1000/T(K)$ (Li <i>et al.</i> , 1998).....                                      | 28 |
| Figure 2-6: EIS testing cell for coated substrate (Akbarinezhad <i>et al.</i> , 2008).....  | 35 |
| Figure 2-7: Salt bridge arrangement for ENM (Mills <i>et al.</i> ).....   | 39 |
| Figure 2-8: Single substrate arrangement for ENM (Mills <i>et al.</i> ).....  | 39 |
| Figure 4-1: EIS testing setup.....  | 44 |
| Figure 5-1: Heat flow and non-reversing heat flow vs T (°C) from DSC for SP2888.....  | 48 |
| Figure 5-2: Heat flow and non-reversing heat flow vs T (°C) from DSC for SP8888.....  | 49 |
| Figure 5-3: SEM image for SP2888.....   | 51 |
| Figure 5-4: SEM image for SP8888.....   | 51 |
| Figure 5-5: SEM image for SP2888 coating pore in with 250X magnification.....   | 52 |
| Figure 5-6: SEM image for SP8888 coating pore with 250X magnification.....  | 52 |
| Figure 5-7: Mapping EDX for SP2888.....   | 53 |
| Figure 5-8: Measured gravimetric water weight fraction for SP8888 and SP2888 in 3% wt NaCl at different temperatures.....                             | 54 |
| Figure 5-9: Impedance from 3 EIS tests, for coating SP2888 in 3% wt NaCl at 30°C.....   | 55 |
| Figure 5-10: Impedance modulus for coating SP2888 in 3% wt NaCl.....  | 56 |
| Figure 5-11: Impedance phase for SP2888 coating in 3% wt NaCl.....  | 57 |
| Figure 5-12: Impedance from 3 EIS tests, for Coating SP8888 in 3% wt NaCl at 30 C°.....   | 57 |
| Figure 5-13: Impedance modulus for SP8888 coating in 3% wt NaCl.....  | 58 |
| Figure 5-14: Impedance phase for SP8888 coating in 3% wt NaCl.....  | 58 |
| Figure 5-15: $Z_{min}$ , $Z_{max}$ , $Z_{\theta=45}$ , and $Z_{f=10}$ Hz for SP2888 in 3% wt NaCl.....  | 59 |
| Figure 5-16: $Z_{min}$ , $Z_{max}$ , $Z_{\theta=45}$ , and $Z_{f=10}$ Hz for SP8888 in 3% wt NaCl.....  | 60 |
| Figure 5-17: EEC used to represent coatings SP8888 and SP2888.....  | 61 |
| Figure 5-18: physical representation of the EEC used to represent the coating systems.....  | 61 |
| Figure 5-19: Goodness of Fit vs T (°C) for SP2888 in 3% wt NaCl.....  | 64 |
| Figure 5-20: The ratio of error arose in the value of calculated Rct and CPE parameters vs temperature for SP2888.....                                | 64 |
| Figure: 5-21: Goodness of Fit vs T (°C) for SP8888 in 3% wt NaCl.....   | 65 |
| Figure 5-22: the ratio of error arose in the value of calculated Rct and CPE parameters vs temperature for SP8888.....                                | 65 |
| Figure 5-23: Calculated volume fraction change due temperature for SP2888 in 3% wt NaCl based on the change in value of coating capacitance (Cc)..... | 66 |
| Figure 5-24: Calculated volume fraction change due temperature for SP8888 in 3% wt NaCl based on the change in value of coating capacitance (Cc)..... | 67 |
| Figure 5-25: Log Rn Vs T (°C) for SP2888 in 3% wt NaCl.....   | 69 |
| Figure 5-26: Log Rn Vs T (°C) for SP8888 in 3% wt NaCl.....   | 69 |

Figure 5-27: Impedance from EIS and Resistance from  $R_n$  ( $\Omega\text{-cm}^2$ ), for SP2888, vs T ( $^{\circ}\text{C}$ )..... 70  
Figure 5-28: Impedance from EIS and Resistance from  $R_n$  ( $\Omega\text{-cm}^2$ ), for SP8888, vs T ( $^{\circ}\text{C}$ )..... 70

## **Acknowledgments**

I would like to express my appreciation and gratitude to all those who supported me throughout my life. My ability to achieve this work would not be possible without them. Of these individuals, the highest mention goes to my dear parents and family, followed by my teachers, instructors, colleagues, and friends. Thank you all for your support, advice and prayers. Each of you, through some or many events in my life, have been a reason for my strength and motivation toward success.

I respectfully thank my supervisor, Professor Akram Alfantazi, for granting me the opportunity to be one of his students in this highly ranked university, and for his continuous support and guidance during my years of study in this program. Also, I really appreciate him sharing some of his vast experience with me, knowledge which I consider to be instrumental in my pursuit of a better career and life.

Special thanks goes to SPC Inc. for their financial support and technical assistance. I also warmly thank all the members of corrosion group for their cooperation, support and friendly sharing of lab equipment and supplies, especially Hung Ha, Ibrahim Gadala, and Faysal Eliyan.

Last but not least, I thank my committee members for their time, comments, and valuable discussions.

Thank you all.

*To those who*

*Loved me and never stopped*

*Gave me and never asked*

*Supported me and never blackballed*

*To my parents, family and friends*

# 1 Chapter 1: Introduction

Oil and gas transportation often requires durable, solid, and yet affordable pipeline systems. Pipeline manufacturers use different types of steel to fill the need for such pipelines. However, steel and most metals are very susceptible to corrosion. They corrode by reacting with their environments. The kinetics of that process varies from one environment to another. While a dry environment can be less corrosive due to lack of electrolyte, moisture enriches corrosion and takes it deep into the body of structures by acting as a transfer medium for corrosive agents. Oxidants, acids, and alkalis can act aggressively on steel if certain circumstances are met.

The consequences of corrosion are very costly. In some cases, the cost can be so expensive if the right precautions were not made. Actually, over the years, corrosion has been the cause for many catastrophes including tank and pipeline explosions, bridge collapses, and mechanical system failures. In the pipeline industry, corrosion failure can cause risk, loss of production, or environmental damage. Thus, to prevent or slowdown corrosion from taking place on steel substrate in pipelines, two techniques are primarily used. These techniques are coatings and cathodic protection.

General principles of cathodic protection are to reduce the corrosion rate of a metallic structure by reducing its corrosion potential, bringing the galvanic potential of the metal to be protected to the immune state level where anodic reactions are impossible for the given circumstances. It can be implemented in two ways: by sacrificial anode and impressed current. Sacrificial anode systems use reactive metals as anodes that electrically connect to the metal to be protected. On the other hand, impressed current systems use an external source of DC power (rectified ac) to

impress a current from an external anode onto the cathodic surface while coatings break corrosion cells and provide shielding from corrosive agents. Coatings should exhibit certain characteristics in order to be considered effective in terms of corrosion protection, Limited water ingression, ionic resistance, and good adhesion are the main characteristics and some mechanical properties are also essential. Actually, coatings need to be able to withstand severe weather including temperatures that may cause them physical changes. Coatings used to protect oil pipelines are often exposed to high temperatures due to the heat generated from crude oil frictions during transfer in the pipeline. With high demands for crude oil or products, pipelines might be operated at even higher flow rates than normal and pipeline temperatures can exceed transition temperature ( $T_g$ ) of the coating.

All thermoplastic materials have an important material property that results from the molecular movement of the side chains of the polymer, the  $T_g$ . It is also known as the glass temperature or glass–rubber transition temperature.  $T_g$  of amorphous polymers is a property which affects many other polymer properties such as heat capacity, the coefficient of thermal expansion, and viscosity. It can be evaluated by several techniques and methods including differential scanning calorimetry (DSC) and temperature modulated differential scanning calorimetry (TMDSC).

In literature, it is not quite clear whether this change in the coating internal structure accompanying the  $T_g$  might affect its corrosion protection properties or not. The purpose of this work is to study the behavior of two coatings, namely SP2888 and SP8888 provided by Specialty Polymer Coatings Inc., at temperatures around their  $T_g$  using EIS in combination with EN testing and other characterization techniques to clarify the role of  $T_g$  on the corrosion protection properties.

## 2 Chapter 2: Literature review

### 2.1 Corrosion in metals

Most metals tend to corrode by reacting with their environments. The tendency to corrode and how fast that corrosion will take place change according to the metal and type of environment. In this chapter we will illustrate the concept of corrosion and some relevant aspects.

#### 2.1.1 Electrochemistry of corrosion

Electrochemistry of corrosion can be explained with the galvanic cell, which employs the concept to convert chemical energy into electrical energy. In the conversion process, a combination of two electrical conductors (electrodes) are immersed in an electrolyte. The electrode at which chemical reduction occurs is called the cathode (Hubbard, 2008; Shreir, 2010). Examples of cathodic reactions are:



The electrode at which chemical oxidation occurs is called the anode (Hubbard, 2008; Shreir, 2010). Examples of anodic reactions are:



## Corrosion Cells:

There are three main types of cells that take part in corrosion reactions.

1. Dissimilar Electrodes Cells. Examples of dissimilar electrode cells include metal-containing, electrically-conducting impurities on the surface as a separate phase, a copper pipe connected to an iron pipe, and a bronze propeller in contact with the steel hull of a ship. Dissimilar electrode cells also include cold-worked metal in contact with the same metal in the annealed state, and a single metal crystal of definite orientation in contact with another crystal of different orientation (Ahmad, 2006a; Talbot, 2008).

2. Concentration Cells. These are cells with two identical electrodes, each in contact with a solution of different composition. There are two kinds of concentration cells. The first is called a salt concentration cell as shown in figure 2-1. For example, if one copper electrode is exposed to a concentrated copper sulfate solution and another to a dilute copper sulfate solution, on short-circuiting the electrodes, copper dissolves from the electrode in to dilute solution (anode) and plates out from the concentrated solution (Eq. 2.2) on the other electrode (cathode). These reactions tend to bring the two solutions to the same concentration. The potential of this potential cell is given by (Eq. 2.16). The second kind of concentration cell, which in practice is the more important, is called a differential aeration cell. This may include two iron electrodes in dilute sodium chloride solution, the electrolyte around one electrode being thoroughly aerated (cathode), and the other de-aerated (anode) by, for example, bubbling nitrogen through the solution. The difference in oxygen concentration produces a potential difference and causes the current to flow (Shreir, 2010; Talbot, 2008). This type of cell is the reason for the pronounced damage at crevices, which is called crevice corrosion. Crevices are common in many engineering designs. The oxygen concentration is lower within crevices and the areas of lower oxygen

concentration (inside the crevice) are anodic with respect to areas of higher oxygen concentration (outside crevices).

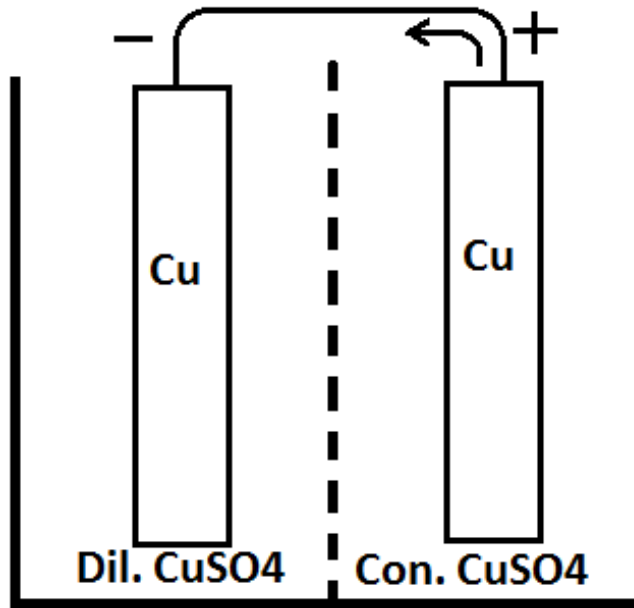


**Figure 2-1: Salt concentration cell redrawn from (Ibrahim, 2005)**

Differential aeration cells can also cause pitting damage under rust and at the water line — that is, at the water–air interface. The amount of oxygen reaching the metal that is covered by rust or other insoluble reaction products is less than the amount that contacts other portions where the permeable coating is thinner or nonexistent, as in figure 2-2 (Ahmad, 2006a; Hubbard, 2008). Differential aeration cells can also lead to localized corrosion at pits (crevice corrosion) in stainless steels, aluminum, nickel, and other passive metals that are exposed to aqueous environments, such as seawater.

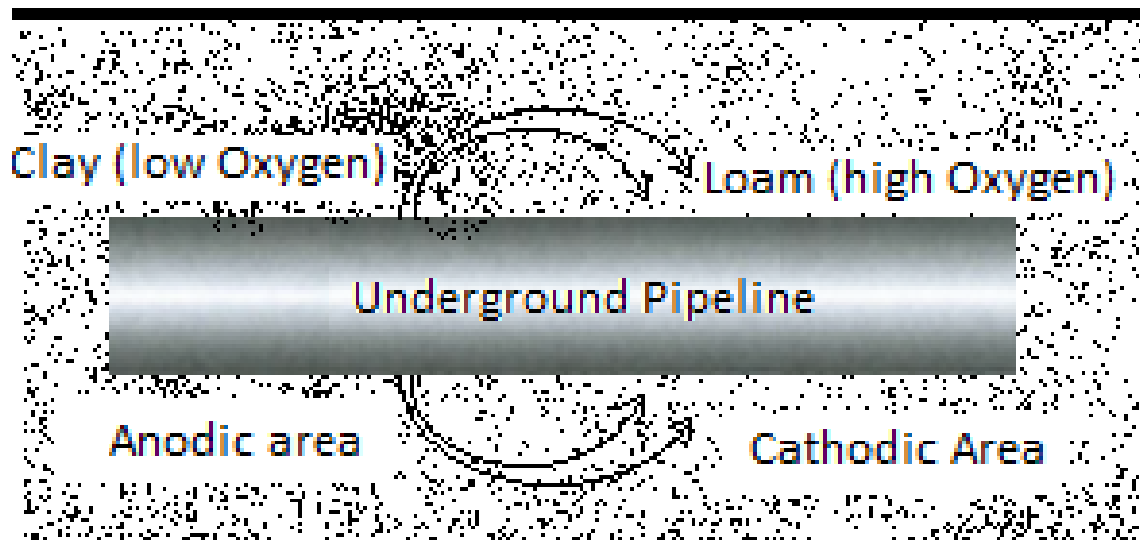


**Figure 2-2: Buried pipeline exhibiting differential aeration cell. redrawn from (Ahmad, 2006a)**

3. Differential Temperature Cells. Components of these cells are electrodes of the same metal, each of which is at a different temperature, immersed in an electrolyte of the same initial composition. Less is known about the practical importance and fundamental theory of differential temperature cells than about the cells previously described. These cells are found in heat exchangers, boilers, immersion heaters, and similar equipment. In copper sulfate solution, the copper electrode at the higher temperature is the cathode and the copper electrode at the lower temperature is the anode. On short-circuiting the cell, copper deposits on the hot electrode and dissolves from the cold electrode. Lead acts similarly, but for silver, the polarity is reversed. For iron immersed in dilute, aerated, sodium-chloride solutions, the hot electrode is anodic to colder metal of the same composition; but after several hours, depending on aeration, stirring rate, and whether the two metals are short-circuited, the polarity may reverse (Shreir, 2010).

In aqueous media, the corrosion reactions are similar to those that occur in a flashlight cell consisting of a center carbon electrode and a zinc cup electrode separated by an electrolyte. An incandescent light bulb connected to both electrodes glows continuously with the electrical energy being supplied by chemical reactions at both electrodes. At the carbon electrode (positive pole), chemical reduction occurs and at the zinc electrode (negative pole) oxidation occurs, with metallic zinc being converted into hydrated zinc ions ( $\text{Zn}^{2+} \cdot n \text{H}_2\text{O}$ ). It was found that the greater the flow of electricity through the cell, the greater the amount of zinc that corrodes. The relationship between current and corrosion is quantitative, as Michael Faraday showed in the early nineteenth century (Cheremisinoff, 1996; Talbot, 2008). This is the relationship now known as Faraday's law (Eq. 2.6).

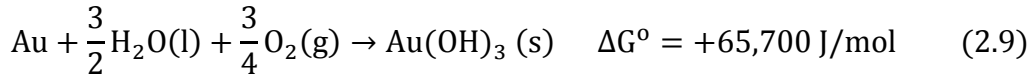
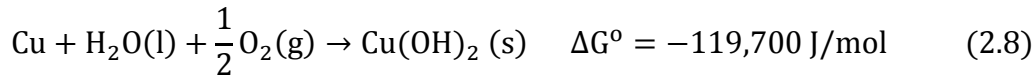
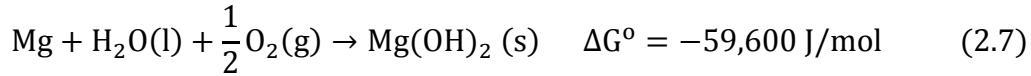
$$W = \frac{mIt}{nF} \quad (2.6)$$

where  $W$  is the weight of reacting metal (g),  $I$  is the current in amperes (A),  $t$  is the time in seconds (s),  $n$  is the number of electrons associated in the reaction and  $F$  is Faraday's constant.

Minute impurities, like iron, embedded in the zinc surface may allow the flow of electricity causing corrosion of zinc. This kind of current is called the local-action current, and the corresponding cells are called local-action cells. As long as the metal remains dry, local-action current and corrosion are not observed. However, on exposure of the metal to water or aqueous solutions, the local-action cells are able to function and are accompanied by chemical conversion of the metal to corrosion products (Corlett *et al.*, 2010).

### 2.1.2 Thermodynamics of corrosion

While some reactions are very favorable in a given environment, others are not. In fact, the tendency for reaction of a metal with its environment, is measured by the Gibbs free-energy change,  $\Delta G$ . The more negative the value of  $\Delta G$ , the greater the tendency for the reaction to proceed (Song, 2012). For example, consider the following reaction at 25°C:



The large negative value of  $\Delta G^\circ$  (reactants and products in standard states) indicates a pronounced tendency for magnesium to react with water and oxygen. On the other hand, in eq. 2.9 the free energy is positive, indicating that the reaction has no tendency to proceed at all; and gold, correspondingly, does not corrode in aqueous media to form  $\text{Au}(\text{OH})_3$  (Ibrahim, 2005). A large negative  $\Delta G$  may or may not be accompanied by a high corrosion rate but, when  $\Delta G$  is positive, the reaction will not proceed at all under the particular conditions described. In view of the electrochemical mechanisms of corrosion, the tendency for a metal to corrode can also be expressed in terms of the electromotive force (EMF) of the corrosion cells that are an integral part of the corrosion process. Since electrical energy (joules, J) is expressed as the product of volts by coulombs, the relation between  $\Delta G$  is in joules and EMF in volts.  $E$  is defined as:

$$\Delta G = -nFE \quad (2.10)$$

where  $n$  is the number of electrons (or chemical equivalents) taking part in the reaction and  $F$  is the Faraday (96,500 C/eq). Accordingly, the greater the value of  $E$  for any cell, the greater the tendency for the overall reaction of the cell to proceed (Ahmad, 2006b; Song, 2012).

Based on thermodynamics, an equation can be derived to express the EMF of a cell in terms of the concentrations of reactants and reaction products. The general reaction for a galvanic cell is:



Meaning that,  $l$  moles of substance  $L$  plus  $m$  moles of substance  $M$ , and so on, react to form  $q$  moles of substance  $Q$ ,  $r$  moles of substance  $R$ , and so on.

$$E = E^{\circ} - \frac{RT}{nF} \ln \frac{a_Q^q \cdot a_R^r \dots}{a_L^l \cdot a_M^m \dots} \quad (2.13)$$

This is the Nernst equation which expresses the exact EMF of a cell in terms of activities of products and reactants of the cell. The activity,  $a_L$ , of a dissolved substance ( $L$ ) is equal to its concentration in moles per thousand grams of water (molality) multiplied by a correction factor called the activity coefficient. The activity coefficient is a function of temperature and concentration and, except for very dilute solutions, must be determined experimentally. If  $L$  is a gas, its activity is equal to its fugacity approximated by the pressure in atmospheres. The activity of a pure solid is set equal to unity (Kendig *et al.*, 2003; Shreir, 2010). Similarly, for water, with concentration essentially constant throughout the reaction, the activity is set equal to unity. Since

the EMF of a cell is always the algebraic sum of two electrode potentials or of two half-cell potentials, it is convenient to calculate each electrode potential separately. For example, for the electrode reaction in eq. 2.14 the cathode potential will be calculated as follows:



$$E_{\text{Zn}} = E_{\text{Zn}}^{\circ} - \frac{RT}{2F} \ln \frac{a_{\text{Zn}}}{[a_{\text{Zn}^{2+}}]} \quad (2.15)$$

where  $\text{Zn}^{2+}$  represents the activity of zinc ions (concentration  $\times$  activity coefficient); Zn is the activity of metallic zinc, the latter being a pure solid and, therefore, equal to unity; and  $E_{\text{Zn}}^{\circ}$  is the standard potential of zinc (equilibrium potential of zinc in contact with  $\text{Zn}^{2+}$  at unit activity). Since it is more convenient to work with logarithms to the base 10, the value of the coefficient  $RT/F$  is multiplied by the conversion factor 2.303. Then, from the value of  $R = 8.314 \text{ J/deg} \cdot \text{mole}$ ,  $T = 298.2 \text{ K}$ , and  $F = 96,500 \text{ C/eq}$ , the coefficient  $2.303 RT/F$  at  $25^{\circ}\text{C}$  becomes  $0.0592 \text{ V}_{\text{SHE}}$  (Corlett *et al.*, 2010; Ibrahim, 2005).

Equation 2.16 describes the potential of differential cell shown in figure 2-1 where h and l notation stands for high and low concentrations.

$$E_{\text{Cu}_h^{2+}/\text{Cu}_l^{2+}} = \frac{RT}{2F} \ln \frac{[a_{\text{Cu}_h^{2+}}]}{[a_{\text{Cu}_l^{2+}}]} \quad (2.16)$$

Pourbaix devised a summary of thermodynamic data in the form of potential–pH diagrams, which relate the electrochemical and corrosion behavior of any metal in water known as

Pourbaix diagrams. They are now available for most of the common metals. They have the advantage of showing, at a glance, specific conditions of potential and pH under which the metal either does not react (immunity) or can react to form specific oxides or complex ions.

From a corrosion engineering perspective, the value of Pourbaix diagrams is in identifying potential–pH domains where corrosion does not occur — that is, where the metal itself is the stable phase. By controlling potential (e.g. by cathodic protection) and/or by adjusting the pH in specific domains identified using Pourbaix diagrams, it may be possible to prevent corrosion from taking place (Kendig *et al.*, 2003) Figure 2-3 shows a Pourbaix diagram for Iron at  $10^{-6}$  m at 25°C. For example, in the potential–pH domain labeled “Fe (immunity),” iron is stable and no corrosion is predicted.

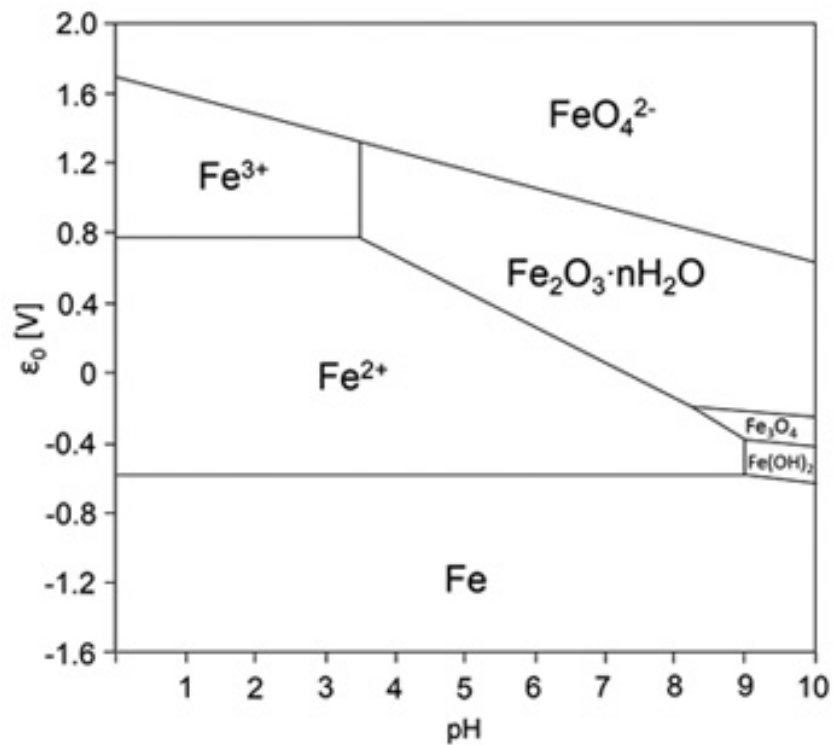


**Figure 2-3: Pourbaix diagram for Iron at  $10^{-6}$  m at 25°C (Beverkog and Puigdomenech, 1996)**

### 2.1.3 Kinetics of corrosion

In practice, we are more concerned with rates of corrosion - that is, with kinetics rather than the tendency of corrosion. Some metals with a pronounced tendency to react (e.g. aluminum) react so slowly that they meet the requirements of a structural metal and may actually be more resistant in some media than other metals that have an inherently less tendency to react (Song, 2012). In general, we must know the equilibrium state of the system before we can appreciate the various factors that control the rate at which the system tends toward equilibrium, that is, the rate of corrosion (Hubbard, 2008; Song, 2012). An electrode is not at equilibrium when a net current flows to or from its surface. The measured potential of such an electrode is altered to an extent that depends on the magnitude of the external current and its direction. The direction of potential change always opposes the shift from equilibrium and, hence, opposes the flow of current, whether the current is impressed externally or is of galvanic origin (Macdonald and Barsoukov, 2005).

Activation polarization can be a slow step in the electrical reaction for which an activation energy in the form of potential is required for the reaction to proceed. When a certain step in a half-cell reaction controls the rate of electron flow, the reaction is said to be under activation charge transfer control and activation polarization occurs. The relationship between activation polarization and the rate of reaction is given by the Tafel equation. Showing an electrode potential in volts in the ordinate and the reaction rate (ampere) in the abscissa is known as Evans diagram. Consider a base metal, such as iron or zinc, placed in an acidic solution; the metal will dissolve at the same rate as hydrogen is evolved and the two reactions mutually polarize each other (Macdonald and Barsoukov, 2005; Talbot, 2008). In an Evans diagram, either current or current density can be plotted against potential. If the ratio of anodic to cathodic areas is taken as unity, current density may be used rather than current. A negligible resistance is assumed

between the anode and cathode. As the change in the anodic and cathodic polarization has the same effect on the corrosion current, the system is considered to be under mixed control (Talbot, 2008). Figure 2-4 shows a schematic of Evans diagram.

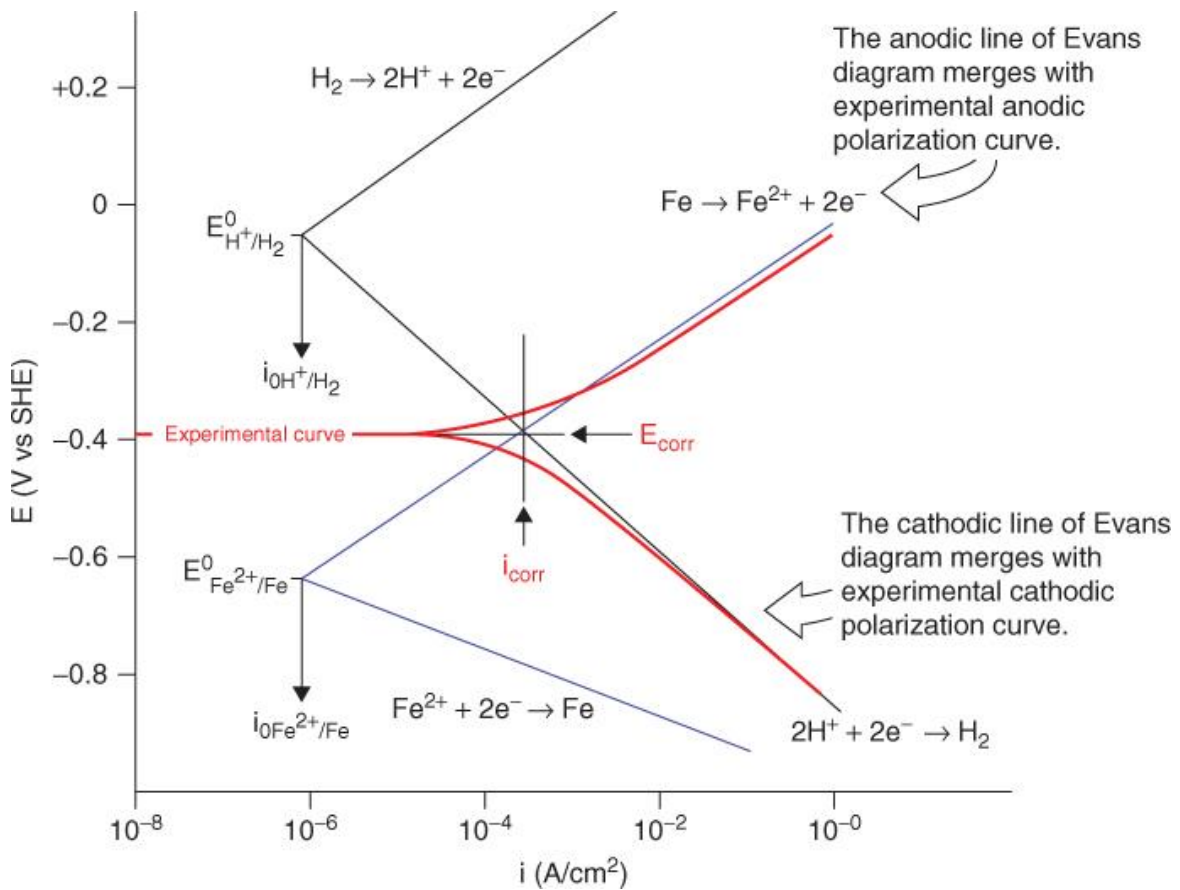


**Figure 2-4: Schematic of Evans diagram for Hydrogen evolution on Iron (Macdonald and Barsoukov, 2005)**

## 2.2 Corrosion protection

To prevent or slowdown corrosion from taking place with metals, many treatments and techniques are used. In the oil and gas industry, a combination of two techniques are often used to protect pipelines located at different environments and terrains. These techniques are coatings and cathodic protection.

### 2.2.1 Coatings

In this section, some aspects of coating materials will be illustrated:

In recent years, the coating industry has shown an environmentally-friendly trend toward the research focused on water-based, powder, and high solid-containing coatings. They have received wide interests by both scientists and industries. Compared to conventional solvent-based coatings, the water-based coatings exhibit a variety of advantages such as inflammability, non-toxicity, and low cost (Peng *et al.*, 2003; Verkholtantsev, 1995). Furthermore, this kind of coating can avoid air pollution caused by the volatile solvents. The preparation of nano-metric polymer latex is the key technology in the manufacturing of water-based coatings. While the latex particles fall into the size of less than 100 nm, the extremely large specific surface area could give rise to a number of novel features, for example, smoothness, strong adhesion, lasting latex dispersion stability, and waterproofness (Peng *et al.*, 2003). In fact, the progress in the nanotechnology of the water-based coatings has widely extended applications in various fields.

Intrinsically-conductive polymers (ICPs), also called synthetic metals, can reach high electrical conductivity. In recent years, a wide variety of ICPs have been tested as coatings that are usually deposited chemically or electrochemically in their pure form on the metal (Zarras *et al.*, 2003). These polymers, when in their doped and conducting condition, are able to protect alloys of steel

from corrosion by an anodic-protection mechanism and they are also able to regenerate the metal oxide layer if the coating is fractured. The presence of an oxide layer at the coating/substrate interface, mainly composed of  $\text{Fe}_2\text{O}_3$  and  $\text{Fe}_3\text{O}_4$ , demonstrates strong evidence that the protection provided by the ICP in the experiment was promoted by the presence of the oxide. On the other hand, studies on doped conducting polymers showed that corrosion was prevented by the aid of a generated electric field, which restricted the flow of electrons from the metal to the outside oxidizing species (Baldissera and Ferreira, 2012; Hasanov and Bilgiç, 2009).

### **2.2.2 Cathodic protection**

Ideally, coatings provide a barrier to separate the pipeline steel from the soil environment. They are the first line of defense against corrosion. However, coatings degrade in various modes during service, contributing to the development of an electrolyte between the coating and the steel to support pipeline corrosion. Over the past 60 years, the pipeline industry has used several coatings including asphalt, coal tar, epoxy, fusion-bonded epoxy (FBE), polyethylene, and urethane coatings. The type of coating on a pipe has an effect on the formation of the environment that causes corrosion and stress corrosion cracking (SCC). As long as pipeline coatings are intact and the pipeline is completely insulated from the surrounding environment, there should be no corrosion but, during service, coatings undergo changes that affect their ability to insulate the pipeline from its environment. Any change in the chemical, physical, or electrochemical properties of external pipeline coatings can be considered as a failure (Fu and Cheng, 2011; Safuadi *et al.*, 2011). Some failures are catastrophic whereas others have little or no effect on the coating performance. However, if the coating fails, cathodic protection (CP) should act as a backup.

The general principle of cathodic protection is to reduce the corrosion rate of a metallic structure by reducing its corrosion potential, bringing the galvanic potential of the metal to be protected to the immune state level where anodic reactions are impossible for the given circumstances. The principle of cathodic protection is implemented in two ways: the sacrificial anode and impressed current. Sacrificial anode systems use reactive metals as anodes that directly electrically connect to the metal to be protected. The natural potential differences between the anode and the metal, as indicated by their relative positions in the galvanic series, generate a positive current to flow in the electrolyte from the anode to the metal. Therefore, the whole surface of the metal becomes more negatively charged and becomes the cathode. The metals that are commonly used as sacrificial anodes, are aluminum, zinc, and magnesium. Current impressed systems use an external source of DC power (rectified ac) to impress a current from an external anode onto the cathode surface (Safuadi *et al.*, 2011). It is difficult to evaluate the effectiveness of a cathodic protection system before the system is applied. People typically depend on experience or trial-and-error. Hence, a method to evaluate the cathodic protection system before deployment becomes important. The use of numerical methods such as boundary element method (BEM) become popular among researchers and corrosion engineers for modeling and solving various corrosion problems (Fu and Cheng, 2011; Ibrahim, 2005).

### **2.3 Polymer coatings**

Pipelines' diversified environment (water, salts, mud, and oxygen) usually tend to aggressively corrode them by completing corrosion cells with their substrates. The consequences of this corrosion can be quite expensive. As an anti-corrosion protection, coatings are usually used with the aid of cathodic protection to break corrosion cells and provide shielding from any corrosion

agents that might exist in the surroundings. However, certain properties should be in those coatings in order to be considered as effective corrosion protection. In this section, we will go through some of these properties.

### **2.3.1 Barrier property**

Organic coatings are frequently used to protect metal surfaces against corrosion. In terms of mechanisms, coatings act as a barrier by slowing down the diffusion of aggressive species towards the metal/coatings interface. generally, the organic coating shows very high electrolytic resistance which impedes the movement of ions between the anodic and cathodic areas (resistance inhibition) (Tüken *et al.*, 2006). The protective ability of a coating system can be assessed by EIS since it measures changes as the protective coatings deteriorate, as they absorb water, and as they permit the substrate to corrode (Le Thu *et al.*, 2006). The ingress of aqueous solutions is likely to result in time-dependent dielectric or chemical changes to the coating/substrate system. These changes during the spectral measurement period produce a Bode plot that has a slope of magnitude slightly less than 1. This capacitive response to the water uptake is commonly characterized by a constant phase element in an equivalent circuit model for the material. Most practitioners measure EIS spectra by starting at the high frequency end of the intended measurement range and progress toward lower frequency measurements with the objective of measuring the maximum number of data points before the system changes since measurements at low frequencies take much longer or are not always possible (Shreepathi *et al.*, 2012; Tüken *et al.*, 2006).

EIS spectra are most often analyzed under the assumptions of linear behavior and steady state equilibrium, which is important if an “equivalent circuit” technique is to be applied. One premise applied to increase experimental rigor is to use the Kramers–Kronig relations to compare the real and imaginary parts of the measurements to eliminate spurious data points. This approach removes data that have been identified as having unstable materials time constants. This approach tends to remove spectral points in the low frequency region which, not coincidentally, have longer periods between sampling. (Le Thu *et al.*, 2006).

### 2.3.2 Sorption

The phenomenon of water absorption is a key parameter in the efficiency of organic coatings in the corrosion protection of metals. Water sorption kinetics usually measured via the gravimetric method using free-standing films and/or by coating capacitance assessment on free or attached coatings. A discrepancy exists between the water uptake kinetics obtained from both methods. Different authors have raised doubts about the validity of either the gravimetric method or the capacitance measurements to determine the real water uptake. In the former case, the argument is that free-standing films may have cracks or defects that cause a gain of mass in addition to the possible loss of mass due to the leaching of pigments and/or polymer (Yang *et al.*, 2005). Meanwhile, the use of capacitance measurements for quantification of the water uptake is based on the large difference between the dielectric constant of water ( $\epsilon_w=80$  at 20 C°) and the dielectric constant of the coating ( $\epsilon_c$  typically between 3 and 8) which allows for small amounts of absorbed water to be detected (Duarte *et al.*, 2009). The capacitance measurement method is widely employed because of its experimental simplicity and its applicability to coatings

supported on metallic substrates, which allows for the study of adhesion effects. The initial slope method is a rather popular procedure for estimating the water uptake in supported coatings:

$$\frac{\text{Log}\left(\frac{C_t}{C_0}\right)}{\text{Log}\left(\frac{C_s}{C_0}\right)} = \frac{2\sqrt{D}}{l\sqrt{\pi}} \sqrt{t} \quad (2.18)$$

In Eq. 2.17; D is the water diffusivity in the coating, l is the film thickness, C<sub>t</sub> is the coating capacitance at time t, C<sub>0</sub> is the (extrapolated) initial coating capacitance, and C<sub>s</sub> is the coating capacitance at saturation (Cao-Paz, 2010).

The water content in organic coatings can be estimated from impedance measurements. Usually, a film of an organic coating is described as a parallel-plate capacitor, meaning that its capacitance is described by:

$$C = \frac{\epsilon\epsilon_0}{d} A \quad (2.19)$$

where  $\epsilon_0$  is the dielectric constant of vacuum, A is the area, and d the coating thickness. Since the relative dielectric constant of polymers is typically in the range of 3–8, being 78.3 for pure water at 25°C, then the absorption of water leads to a rise in the  $\epsilon$  and thus a higher capacitance (Giacomelli Penon *et al.*, 2007).

Castela and Simoes (2003) have described the mixed  $\epsilon$  for a three-component system consisting of a continuous phase containing randomly-distributed water and air by:

$$\epsilon_f = \epsilon_s^{\phi_s} \epsilon_w^{\phi_w} \epsilon_a^{\phi_a} \quad (2.20)$$

where  $\phi$  stands for the volume fraction, and the subscripts s, w, and a correspond to the solid polymer, the water (liquid phase), and air. Since  $\epsilon_a = 1$  and assuming that leaching does not occur and not changes happening in the polymer ( $\phi_s \sim \phi_{s,0}$ ), it results in:

$$\frac{\epsilon_f}{\epsilon_{f,0}} = \frac{\epsilon_w^{\phi_w}}{\epsilon_w^{\phi_{w,0}}} \quad (2.21)$$

where subscript 0 corresponds to the instant of immersion, i.e.,  $t = 0$ . Assuming that the film is dry at the instant of immersion, then  $\phi_{w,0} = 0$  and

$$\phi_w = \frac{\text{Log}\left(\frac{\epsilon_f}{\epsilon_{f,0}}\right)}{\text{Log}\epsilon_w} \quad (2.22)$$

This deduction was made by Brasher and Kingsbury. The Brasher–Kingsbury law is the most widely used relationship for the quantification of the water ingress into organic coatings. The equation being normally used is:

$$\phi_t = \frac{\text{Log}\left(\frac{C_t}{C_0}\right)}{\text{Log}\epsilon_w} \quad (2.23)$$

In this Eq.,  $\phi_t$  is the volume fraction of water in the coating at time t,  $C_t$  is the coating capacitance at time t,  $C_0$  is the initial coating capacitance (Castela and Simoes, 2003).

The determination of the water uptake can be easily performed gravimetrically. Assuming an ideal Fickian process, the sorption data for plane sheet geometry is represented by this equation.

$$\frac{M_t}{M_s} = 1 - \frac{8}{\pi^2} \sum_{n=0}^{\infty} \frac{1}{(2n+1)^2} \exp\left[-\frac{(2n+1)^2 D \pi^2 t}{l^2}\right] \quad (2.24)$$

where  $M_t$  is the amount of absorbed water at time ( $t$ ),  $M_s$  is the amount of water absorbed at saturation,  $l$  is the thickness of the free-standing specimen, and  $D$  is the diffusion coefficient which is considered to be constant over the exposition time. The same relation holds for a supported coating with a thickness of  $l$  changing the denominator of the argument of the exponent  $l^2$  to  $4l^2$ .

At sufficiently short times, the water uptake is proportional to the square root of time.

$$\frac{M_t}{M_s} = \frac{4\sqrt{D}}{l\sqrt{\pi}} \sqrt{t} \quad (2.25)$$

for a free-standing film and

$$\frac{M_t}{M_s} = \frac{2\sqrt{D}}{l\sqrt{\pi}} \sqrt{t} \quad (2.26)$$

for a supported film (Castela, 2003).

Despite its simplicity, the gravimetric method notably suffers from the fact that soluble components, either initially present in the dried film or in situ generated owing to hydrolytic instability, can be easily washed out during the immersion time. The determination of water content of coatings by impedance spectroscopy is based on the increase in the permittivity and, consequently, in the measured capacitance of the material that accompanies water absorption. (Nguyen, 2005).

Coated systems are seldom tested in a rigorous fashion to eliminate that transient nature. One method, now available, is to use a room temperature ionic liquid ( $D_2O$ ) to replace the aqueous electrolyte in the measurement cell so that the water in the coating film may be investigated independently (Hinderliter and Croll, 2009).

### 2.3.3 Adhesion

Very good adhesion is required between the coatings and the metal to prevent corrosion delamination. Corrosion protection and adhesion of the film are two related phenomena, but it is not clear if loss of adhesion is a consequence of the corrosion process or vice versa, and the relationship between adhesion and corrosion still remains a subject open to discussion. (Le Pen *et al.*, 2000). Polymer–metal bonding has several applications in industries. However, due to their low surface energy, many polymers exhibit poor adhesion to steels. In order to enhance this adhesion, surface modifications involving mechanical roughening, anodization, and wet chemical primer treatments have been applied. In previous studies, atmospheric pressure plasmas (Rouw, 1997) have been successfully demonstrated to improve adhesion of silicone elastomer to steel a plasma-polymerized primer layer formed from polyhydrogenmethylsiloxane (PHMS) and tetraethoxysilane (TEOS) was used. It has been reported previously that for an atmospheric plasma deposited primer layer, surface roughness, interfacial chemistry, and thickness all have significant effects on adhesion (Nwankire and Dowling, 2010).

The strength and stability of the adhesion to the substrate may be a critical factor in the long-term epoxy resin performance. However, there is an abundance of practical evidence that adhesion to metal is partially or totally lost when the epoxy coating is exposed to water or high

humidity. Such exposure may quickly lead to coating detachment. This phenomenon of wet-adhesion loss, which is also known for other binder systems, has been investigated by many coating scientists. It can be attributed to the action of water that penetrates the coating down to the polymer/metal interface or to compounds resulting from electrochemical decomposition of water at this interface. In both cases, the bond between the hydroxyl or other polar groups from the resin and the metal oxide layer on the substrate is destabilized (Rouw, 1997).

Understanding the adhesion of protective polymer coatings to substrates is critical for the prediction of coating performance. Different methods to measure the adhesion of thin coatings exist, but experimental measurements of polymer adhesion are qualitative or problematic. For instance, ASTM D3359 describes procedures for scribing a cross hatch pattern in the coating and then applying and removing tape. The response is classified according to the amount of coating area that is detached. Pull-off tests described in ASTM D4541 provide a quantitative assessment of adhesion, but they are often not reproducible; the glue used to attach the dolly can affect the coating, and failure often does not occur at the coating/substrate interface. Additionally, testing wet adhesion, i.e. adhesion of films immersed in aqueous solutions, by standardized tests such as the pull-off test is difficult because of problems like attaching the dolly to a wet coating. Seong and Frankel (2012) have developed a standardized scratch test for testing the adhesion of hard coatings such as alumina, titanium nitride, and diamond-like carbon by dragging a stylus along the coating surface with increasing normal force and measuring the load at which the coating fails in a brittle fashion. They have used atomic force microscopy (AFM) to test adhesion of ultra-thin coatings (<2 nm) by measuring the friction signal. A controlled force was applied between the AFM cantilever tip and sample surface. The tip was mastered across the edge of an applied thin polymer coating. The tip moved from an uncoated region across the edge of the

coating with the cantilever aligned in the direction of scratching. Coating adhesion was determined by the number of raster scans required to remove the coating at different forces.

#### **2.3.4 Glass transit temperature**

All thermoplastic materials have an important material property that results from the molecular movement of the side chains of the polymer, the  $T_g$ .  $T_g$  of amorphous polymers is the most important property which affects many other polymer properties such as heat capacity, coefficient of thermal expansion, and viscosity. It can be evaluated by several techniques and methods including DSC, TMDSC, dynamic mechanical analysis (DMA), dielectric analysis (DEA), and thermo-mechanical analysis (TMA). Depending on the technique and the operating conditions, different parameters and terms related to the  $T_g$  are used. Particularly the  $T_g$  obtained by TMDSC and DMA are referred to as dynamic  $T_g$  ( $T_{gd}$ ). (Gracia-Fernández *et al.*, 2010; Kim *et al.*, 2007).

There have been numerous attempts to estimate  $T_g$ 's for polymers on the basis of quantitative structure–property relationships. There are two kinds of approaches, the empirical method and the theoretical estimation. Empirical methods correlate the target property with other physical or chemical properties of polymers, for example: group additive property (GAP). The most widely referenced models of the theoretical estimations have been produced by Bicerano. Bicerano produced a regression model with a correlation coefficient (R) of 0.9749 and a standard error(s) of 24.65 K to relate  $T_g$  with the solubility parameter and the weighted sum of 13 structural parameters for the data set of 320 polymers. Katritzky introduced a model with an  $R^2$  of 0.928 for 22 medium molecular weight polymers using four parameters. (Liu *et al.*, 2007).

A practical model can be constructed based on the RBF neural network architecture for a set of molecular weight polymers. The neural network models are produced based on the special fuzzy means training method for RBF networks that exhibits small computational times and excellent prediction accuracies (Afantitis *et al.*, 2005).

Yang *et al.* investigated the effects of moisture on  $T_g$  of a polyurethane shape memory polymer (SMP) filled with nano-carbon powders. Experimental results showed that the  $T_g$  can be reduced effectively by water immersion. The absorbed moisture interacts with the polymer chains and thus improves their mobility, resulting in the decrease of  $T_g$ . This phenomenon holds until the polymer is saturated by water. Moreover, results indicate that the added carbon powders have tendency to lower the  $T_g$ . They also found that the change of transition temperature is reversible by heating or dehydrating since the removal/absorption of moisture is only a physical process (Yang *et al.*, 2005). However, numerous equations have been offered to describe the plasticization effect of glassy polymers, i.e. the  $T_g$  depression as a function of plasticizer concentration. These equations have been derived from the free volume concept or from thermodynamic arguments. The simple rules of mixing have been stated by the Fox and Gordon-Taylor equations. They neglect specific interactions between the polymer and the plasticizer, inferring a complete uniformity of intermolecular forces. In practice, the plasticization effect often involves the specific interactions or excess volume formation upon mixing the polymer and the plasticizer (Feldstein *et al.*, 2001; Righetti *et al.*, 1992).

It was found that the  $T_g$  of an immersed coating can be measured by electrochemical means. As resistance measured by ENM and DC methods or  $|Z|$  at low frequency from EIS. The  $T_g$  measured electrochemically in immersion was a  $T_g$  of a wet film and, therefore, was lower than

the  $T_g$  of dry film. However, DSC measurements on free electrolyte-wet films yielded the same  $T_g$  values as electrochemically determined (Li *et al.*, 1998; Perera, 2002).

## 2.4 Role of temperature

### 2.4.1 Barrier property

Films of commercial epoxy coatings with iron oxide pigment were evaluated by Angeles *et al.*, (2012) at temperatures of 25, 65, 85, and 100°C, based on the degradation parameters measured by EIS. The results showed that there was no damage in their protective capacity over time. The fact that the plots do not show the same behavior is evidence of the thermal effect each sample went through. This was inferred after looking at the Bode plots because in the original sample (at 25°C), an impedance value at the order of  $10^7$  Ohm-cm<sup>2</sup> and more than one time constant can be observed. On the other hand, the sample that was aged at 85°C showed a capacitive behavior with impedance range of  $10^{10}$  Ohm-cm<sup>2</sup> and phase angles close to 90°. In this case, the high impedance was attributed to the oxides on the metal-paint interface which occlude the pores blocking the electrolyte permeability. On the sample aged at 65°C, a slight increase in the impedance value after five cycles was observed. However, the phase angle showed seven time constants, which was attributed to the formation of oxides on the metal surface. When the heating was finished, the impedance went back to its original value of  $10^7$  Ohm-cm<sup>2</sup>, keeping a high resistance. However, the sample aged at 100C showed a performance different to that expected for an insulated coating, although the impedance value was  $10^7$  Ohm-cm<sup>2</sup>, the phase angle showed at least two time-constants. Also, Bierwagen *et al.* (1996) examined films using EIS measurements of paint films showing Bode and Nyquist plots of their data for the same films at various temperatures. They saw only decreases in film resistance and increases in film capacitance with temperature (using only four temperatures) after an initial 4 h soak in a 3%wt

sodium chloride (NaCl) electrolyte at 25°C. When higher temperatures were applied, resistance decreased and capacitance increased to a larger extent. This was interpreted as film degradation and nothing was noted with respect to film thermal transitions. Thermal effects on FBE powder coated on steel exposed to NaCl solutions were also studied by measuring EIS,  $R_n$ , and  $R_{DC}$  at temperatures from 28°C to 95°C. Temperatures were increased slowly (5°C per 20 min) and held at the tested temperature for 15 min before each measurement to ensure equilibrium. The EIS results in Nyquist form, showed  $Z''$  vs  $Z'$  shrunk drastically as temperature increased. While in Bode plot form,  $|Z|$  leveled off at the low-frequency end to lower and lower values as T increased. In fact, the logarithm of all three measures ( $R_{DC}$ ,  $R_n$ , and  $|Z|_{\text{low frequency}}$ ) of the resistance properties of the coating showed that they were following an Arrhenius type of temperature dependence where the log (property) is linear in  $1/T$  as shown in Figure 2-5:  $R_n$ ,  $Z$  and  $R_{DC}$  at 3%wt NaCl for FBE coating Vs  $1000/T(K)$  (Li *et al.*, 1998). This means the property is controlled by activation energy. However, this linear behavior was exhibited in two distinct temperature ranges intersecting at approximately the same temperature for all the three measures. On the other hand, Rezaei *et al.* (2010a). studied the influence of temperature on the impedance of coatings immersed in distilled water. The diffusion behavior and coating resistance at 75°C shows a significant drop in comparison to that of 25°C. They concluded that the impedance spectra of some coatings are especially sensitive to temperature but, in contrast, some high-impedance coatings exhibit little change in the impedance when exposed to distilled water over a temperature range of 25–80°C. Li *et al.* (1998), using EIS monitoring and an embedded sensor, showed that the resistance of both the coating and coating/metal interface decrease with temperature and the corrosion processes increase, although sudden increases in the coating

impedance were reported. This increase is caused by the clogging of the pores with corrosion from the metal substrate.

The coating barrier properties decrease at higher temperatures due to the increase of electrolyte diffusion rate through the coating film as well as the film aging which decisively influences the corrosion reaction at the coating/metal interface. In addition, the loss of this barrier property is more significant in the presence of ions. In fact, corrosion on samples immersed in 3%wt NaCl solution at 75°C was detected on the 3rd day while the first detection of the corrosion process was on the 52nd day for the test performed at 25°C (Rezaei *et al.*, 2010a).

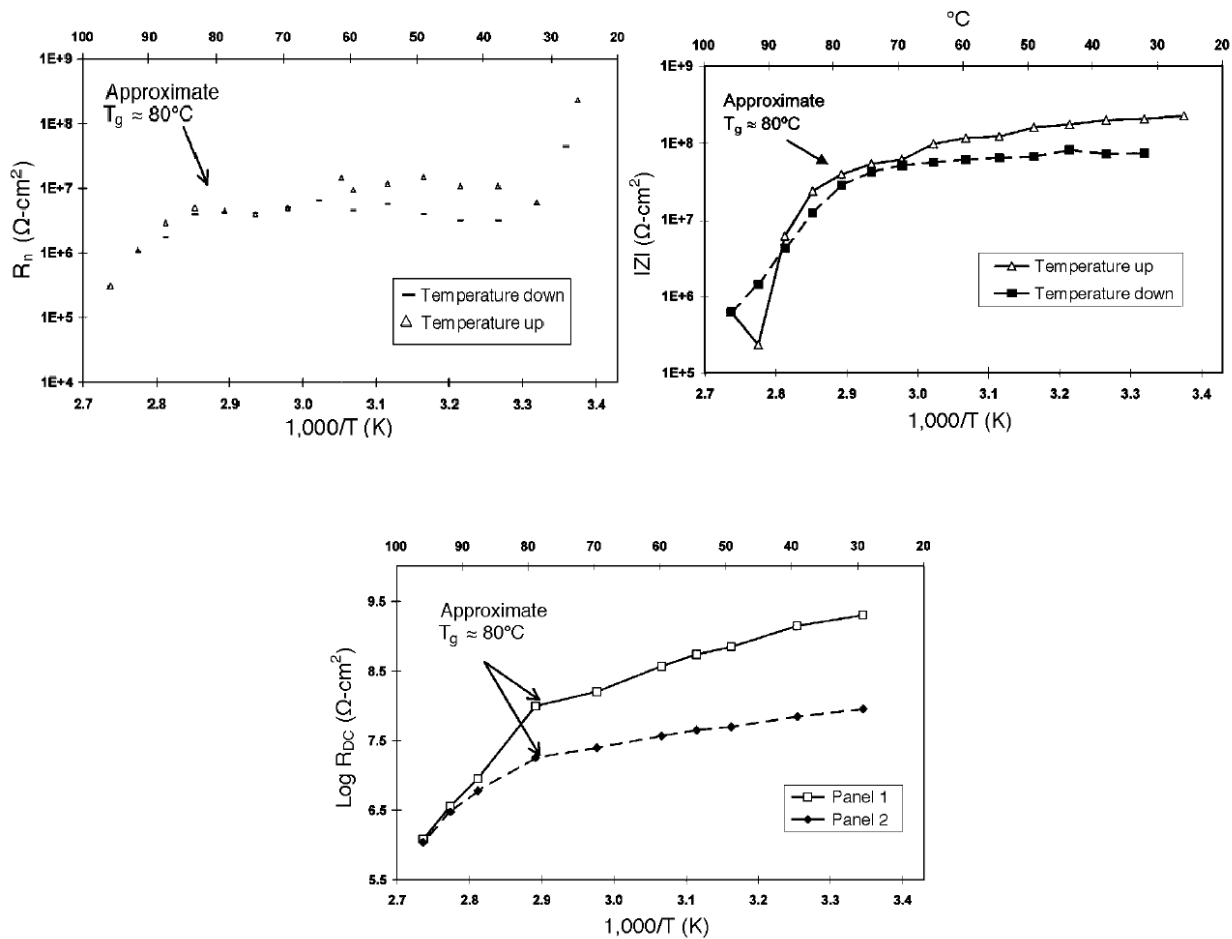


**Figure 2-5:  $R_n$ ,  $Z$  and  $R_{DC}$  at 3%wt NaCl for FBE coating Vs  $1000/T(K)$  (Li *et al.*, 1998)**

## 2.4.2 Sorption

Philippe *et al.* (2004), in their work, used FTIR/ATR to study the sorption and desorption of water into a series of cured epoxy resins at temperatures of 10-50°C. At lower temperatures (18–35°C) well below the  $T_g$ , the sorption was a two-stage process. This is likely associated with changes in water clustering among the distributed ‘voids’ in the glassy polymer associated with chain relaxation at extended times. For higher temperatures (35–50°C), the sorption was a single Fickian diffusion process, even though the polymer is not above the  $T_g$  (measured by DSC to be 50°C) for the dry polymer. An increased diffusion coefficient was also observed as the temperature increased. Table 2-2 shows diffusion coefficients at a different temperatures. However, it seems that an in-depth understanding of the link between the  $T_g$  and the temperature dependence on structural relaxation or diffusion remains elusive. D<sub>2</sub>O was used as a penetrant to measure the diffusion coefficient for highly dense epoxy matrices which was not possible with water.

**Table 2-1: Water Diffusion Coefficients and sorption profile for epoxy resins (Philippe *et al.*, 2004)**

| Polymer temperature (°C) | Sorption profile | Diffusion coefficients ( $10^8/\text{cm}^2 \text{ s}^{-1}$ ) |
|--------------------------|------------------|--|
| 22                       | Two-stage        | $D_1 = 1.8 \pm 0.2$ , $D_2 = 2.3 \pm 0.2$                    |
| 30                       | Two-stage        | $D_1 = 8.5 \pm 0.8$ , $D_2 = 1.1 \pm 0.1$                    |
| 35                       | Two-stage        | $D_1 = 5.1 \pm 0.5$ , $D_2 = 1 \pm 0.1$                      |
| 40                       | Fickian          | $D = 2.1 \pm 0.2$  |
| 45                       | Fickian          | $D = 3.3 \pm 0.3$  |
| 50                       | Fickian          | $D = 4.5 \pm 0.4$  |

It is worth considering that the saturation time is defined as the time when the coating capacitance reaches a steady value. The water diffusion coefficients of coatings with good barrier properties that have been reported in literature are in the range of  $10^{-8}$  to  $10^{-12}$  cm<sup>2</sup>/s at room temperature. According to Rouw and Nguyen *et al.*, water uptake calculated from EIS is higher than gravimetric measurements. Gravimetric measurements show 1.4% water uptake while EIS measurements give 7–14% water uptake. One of the explanations is offered by Stafford *et al.* (2006), who attributed the difference to the shape of water inclusions. Guermazi *et al.* (2009) has studied Polymer based on high density polyethylene (HDPE) after being immersed in synthetic sea water at several temperatures. Three values of temperature were undertaken: 23, 70, and 90°C. Sorption kinetics was studied through water absorption rate response at those temperatures. Similarly, diffusion coefficients of solvent molecules in the coating samples were determined. In the first approximation, there was a diffusion process of solvent molecules into polymer samples, which is characterized by a fast increase in the sample weight with time. Therefore, an equilibrium stage was reached after a limited period. Finally, there was a remarkable weight loss process which was superimposed to water sorption. Moreover, varying temperature has shown that this parameter enormously influences the water sorption response of the studied material.

Increasing the aging temperature affects the initial increase of the sample weight, the equilibrium stage, and the weight loss process (Stafford *et al.*, 2006). In fact, the increase in the temperature leads to the acceleration of the diffusion process, reduction in the duration of the equilibrium stage, and a rise in the equilibrium uptake. The linearity of the initial stage in the weight gain against  $t^{1/2}$  curves was used to determine the diffusion coefficients. On the other hand, the last stage that corresponds to the decrease of the mass gain ratio or decrease of the sample weight

may be ascribed to many phenomena such as the reorganization of polymer chains, the washing phenomena, and the migration of cross-linking agents to the surface during aging process or the extraction of low molecular weight compounds (Guermazi *et al.*, 2009). Against what has been mostly reported in literature in the early days Kittelberger and Elm, 1946 (Rezaei *et al.*, 2010a) have reported lower water uptake of the film for the salt solutions and attributed that to the osmotic pressure. At 75°C, the ion presence in NaCl solution affects the trend of the curve and the saturation phase. In spite of the coating thickness difference, the water uptake of coated samples in distilled water both at 25°C and at 75°C are similar during the first 48 h. The trends of the reduction of impedance of coatings are similar at both temperatures during the initial days but, then since the corrosion process occurs at the coating/steel interface at 75°C, the loss of coating resistance is very high and after 45th day. Reduction of resistance of coated samples immersed in 3%wt NaCl solution at 75°C is more than the one at 25°C (Rezaei *et al.*, 2010a).

### **2.4.3 Adhesion**

Hydrolysis of coating bonds, named cathodic disbanding, is caused by alkaline pH at the cathode. The alkaline pH is first of all produced by oxygen reduction below the coating. However, this can only take place if cations are migrating between anodic and cathodic areas to keep the charge in balance. Moreover, it needs an anode to establish the galvanic element, the formation of which is enhanced in salt solution compared to distilled water. Leng *et al.* (1998) proved that two factors such as the concentration of cations and anions and the thickness of the oxide layer are of particular importance to the delamination process. In the presence of ions, a passive layer can be produced in an alkaline electrolyte which is the delamination zone. In addition, the type and concentration of the cation influence the delamination kinetics. On the

other hand, the salt spray test results of intact coating show a few blisters, according to ASTM D-714, after 5 months of exposure time. The pH of liquid in the blister was 14 and a spot of rust was observed in the center. The results of the salt spray test confirm that cathodic blistering, which occurs on the coating, is produced by cathodic reaction around the pathways of film, which is considered as the anode area (Rezaei *et al.*, 2010a).

## **2.5 Testing Methods**

To evaluate the effectiveness of the corrosion protection behavior of polymer coatings, some commonly used techniques will be illustrated:

### **2.5.1 Electrochemical impedance spectroscopy (EIS)**

Electrochemical impedance spectroscopy has been widely used to study corrosion protection by organic coatings (Cantini *et al.*, 2000). It has been widely used in the investigation of the degradation of polymer-coated metals because of its ability to measure high impedance systems and to provide abundant information (Szociński *et al.*, 2010; Xia *et al.*, 2012). Advantages of this technique over DC and conventional techniques include the absence of any significant perturbation to the system and its applicability for assessment of low-conductivity media such as polymers (Cantini *et al.*, 2000). Also, it is a non-destructive technique and has the ability to reveal early signs of coating degradation (Szociński *et al.*, 2010).

Effects of elevated temperature and cyclic temperature changes has been the focus of many EIS investigations in the field of polymer coatings. EIS was used for the identification of organic coating degradation caused by factors of mechanical origin such as tensile stress or abrasion. EIS was also found to be a useful tool in monitoring polymer coating degradation on accelerated

aging involving UV radiation, mechanical deformation, and thermal cycling (Szociński *et al.*, 2010). Oliveira and Ferreira (2003) used electrochemical impedance spectroscopy to rank paint systems with respect to their susceptibility to degradation when tested in 3%wt NaCl solution at ambient and elevated temperatures. However, detection of onset degradation allows finding the interaction between particular regions of the polymer coating with the environment and identification of the weakest points in the coating structure, which are the ones determining the resistance of the entire protective layer. Obtaining such information can contribute to the improvement of the coating material by strengthening the weakest points being the preferred sites of degradation. Classical impedance measurements reveal a shortage in this field so it is not possible to spatially localize the spots of coating degradation. (Szociński *et al.*, 2010).

EIS has some significant drawbacks. At low frequencies, where under-film corrosion reactions are probed, experimental difficulties and time constraints can complicate precise determination of the charge-transfer resistance ( $R_{ct}$ ) and the double-layer capacitance ( $C_{dl}$ ). Additionally, the Warburg impedance may exhibit a masking effect and inductive loops or new time constants are sometimes observed. Further, due to the long measurement of time required, both the corrosion rate and corrosion potential can change during the experiment. There has also been no evidence that  $R_{ct}$  can be equated to the polarization resistance ( $R_p$ ) and used in the Stern-Geary equation to calculate the under-film corrosion rate. (Cantini *et al.*, 2000). However, Xia *et al.* (2012) observed a linear relationship between  $f_{\theta, \max}$  and  $R$ , where  $f_{\theta, \max}$  is the frequency at which the phase angle is maximum and  $R$  is the coating resistance. The relationship may serve as a criterion for fast evaluation of coating performance since  $f_{\theta, \max}$  can be measured easily. Shiro and Shirohi proposed the concept of breakpoint frequency,  $f_b$ , a frequency at which the phase angle first fell to  $45^\circ$  and found a good correlation between the breakpoint frequency and the

disbonded area of coating to the metal. Zuo *et al.* (2008) used the variation of the phase angle at 10 Hz to evaluate the coating performance and they found that the phase angle parameters at 10 Hz can reflect the degradation degree of coatings. The advantage of the methods above is that the parameters are usually obtained in high frequency domains of the impedance spectrum, so the measurements in low frequency domains and accurate analysis for EIS data may be avoided.

The EIS method uses a fixed DC potential accompanied by an AC current at low perturbation under different frequencies. Electrochemical equivalent circuit (EEC) is a classical analytical method to process EIS data. Through the analysis of parameters from EEC fitting, coating resistance, coating capacitance, polarized resistance, and double-layer capacitance can be obtained. However, there are always some errors when using equivalent circuits to simulate the EIS results for complicated coating system. (Xia *et al.*, 2012; Zuo *et al.*, 2008). Also, data scatter possibly exist during the measurement at low frequency. In addition, an equivalent circuit involving three or more circuit elements can often be rearranged in various ways and still yield exactly the same impedance (Cantini *et al.*, 2000). When an artificial hole is present through a coating, this point becomes a main electrochemical response site, since its impedance is much smaller than the impedance of the flawless area. Inversely, long immersion of thick coatings under CP without an artificial defect area can require several years before a significant degradation can be detected. Definitely, this is incompatible to industrial requirements.

The EIS measurements have another definite advantage compared with the adherence measurements of coating. It is not invasive and allow monitoring of the same specimens for a long period. Though, it presents some drawbacks. The pH evolution under cathodic protection with very thick organic coatings makes accurate EIS measurements difficult to realize because of

huge impedance values associated with such coatings. (Le Thu *et al.*, 2006). Figure 2-6: EIS testing cell for coated substrate (Akbarinezhad *et al.*, 2008)

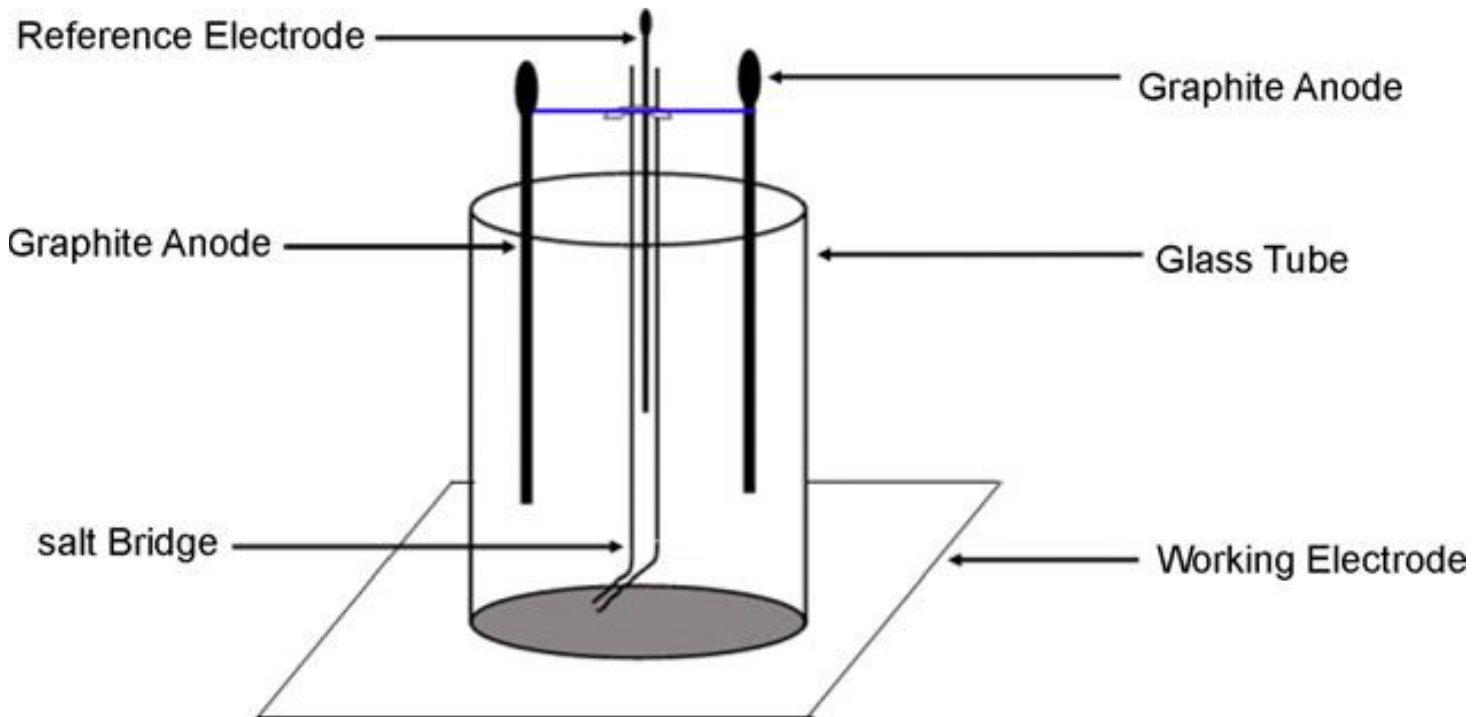


**Figure 2-6: EIS testing cell for coated substrate (Akbarinezhad *et al.*, 2008)**

### 2.5.2 Electrochemical Noise

When a metal electrode is immersed in a corrosive electrolyte, anodic and cathodic reactions occur simultaneously on its surface. Generally, the anodic reaction involves the oxidation of the metal-to-metal ions, which are released into the environment, while the cathodic reaction involves the reduction of species present in the environment, such as molecular oxygen or hydrogen ions. The rate at which the anodic and cathodic reactions proceed can fluctuate with time but, overall, the rate of the anodic and cathodic reactions are balanced at open-circuit potential in order to preserve electro-neutrality (Curioni *et al.*, 2013; Mills *et al.*, n.d.). Generally,

the rate of the anodic reaction increases with increasing electrode potential, while the rate of the cathodic reaction increases with decreasing electrode potential. Consequently, the average corrosion potential represents the potential at which the average rates of anodic and cathodic reaction are balanced. However, if, for example, a rapid increase of the anodic reaction rate proceeds, some of the charge generated by metal oxidation can be transiently stored in the capacitance that is generated due to charge separation at the double-layer capacitance, before being consumed by the cathodic reaction on the electrode surface, known as an anodic event. As a result, a fluctuation in the corrosion potential is observed; initially, the potential decreases rapidly due to the charging of the double layer capacitance and, subsequently, it recovers as a result of the progressive consumption of charge by the cathodic reaction (*Lowe et al.*, 2003). Depending on the material-environment combination, anodic or cathodic events can be relatively large and occasional, such as for a passive material suffering metastable pitting, or relatively small and frequent, such as for materials undergoing active corrosion (*Cottis*, 2007). Consequently, larger potential and current transients are observed in the first case compared with the second case. Thus, the corrosion type can be determined by analyzing the potential and current noise by statistical methods. For two galvanically coupled electrodes comprising equal areas of the same material, when one event occurs on the surface of one electrode some charge associated with that event is consumed on the same electrode and some charge is consumed on the other electrode. In this case, one-half of the charge generated on one electrode is consumed on the same electrode, and one-half of the charge is consumed on the other electrode. If the galvanic coupling between the two electrodes is realized with a zero-resistance ammeter, the coupling current can be measured simultaneously with the potential of the electrodes (*Curioni et al.*, 2012).

The principal aim of ENM when applied to the assessment of organic coatings is to obtain a single result: the noise resistance ( $R_n$ ). Electrochemical noise can be described as naturally-occurring fluctuations in potential and current around a mean value in an electrochemical cell. From these fluctuations, the derived parameter voltage noise and current noise can be obtained. These parameters are used in an Ohms Law relationship to calculate the desired value — the noise resistance. Therefore, ENM is an electrically non-intrusive method because during the test, only natural fluctuations of current and potential are measured. ENM does not need any activation signal. It is also a very sensitive method. Another advantage is the relatively short time of a single measurement (only a few minutes). The value of noise resistance allows us to assess the protectiveness of paint coatings. Bacon *et al.*, while doing extensive measurements, found a relationship between the resistance value and the protection afforded by the coating to the substrate. Less than  $10^{-6} \text{ cm}^2$  indicates poor corrosion protection, more than  $10^8 \text{ ohm cm}^2$  good corrosion protection, a value between  $10^6 \text{ ohm cm}^2$  and  $10^8 \text{ ohm cm}^2$  shows an intermediate level of corrosion protection (Cottis, 2006).

For ENM measurements, three electrodes are required: two working electrodes (WE1 and WE2, between these, the current is recorded by a zero resistance ammeter (ZRA) at regular intervals) and one reference electrode, RE. Potential is measured between RE and the working electrode couple. Current and potential are registered simultaneously. The reference electrode must have a stable potential. Therefore, SCE (saturated calomel electrode) is most commonly chosen in laboratory measurements. Eden *et al.* proposed an experimental setup for measuring EN that enables quantities known as the noise resistance and the spectral noise impedance to be computed.

These quantities have been linked to the electrochemical equivalent impedance of the electrodes, which can provide much valuable information regarding the corrosion process and, in particular, the rate of corrosion. Bertocci *et al.*, and Mansfeld and co-workers have observed good experimental correlation between the spectral noise impedance and the magnitude of the electrode impedance determined by AC polarization techniques. The noise resistance and spectral noise impedance have been shown to be helpful in corrosion studies in many practical research cases (Lowe *et al.*, 2003). A variety of methods are available for electrochemical noise analysis, ranging from techniques based on the statistical analysis of the current and/or potential signal, fast Fourier transform or wavelet transform-based analyses, and others. Each method has specific advantages for the study or monitoring of a particular corroding system. Whatever the approach for the analysis, if both current and potential noises need to be acquired, generally two working electrodes and a third reference electrode are used (Curioni *et al.*, 2012). Figure 2-7: Salt bridge arrangement for ENM (Mills *et al.*) and Figure 2-8: Single substrate arrangement for ENM (Mills *et al.*)

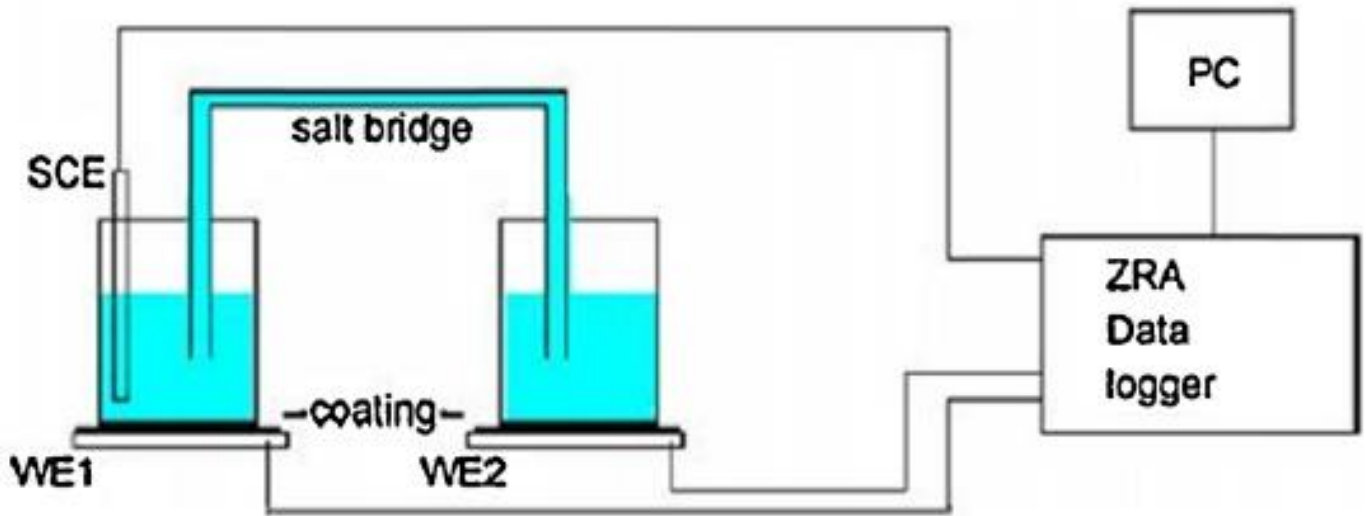


Figure 2-7: Salt bridge arrangement for ENM (Mills *et al.*)

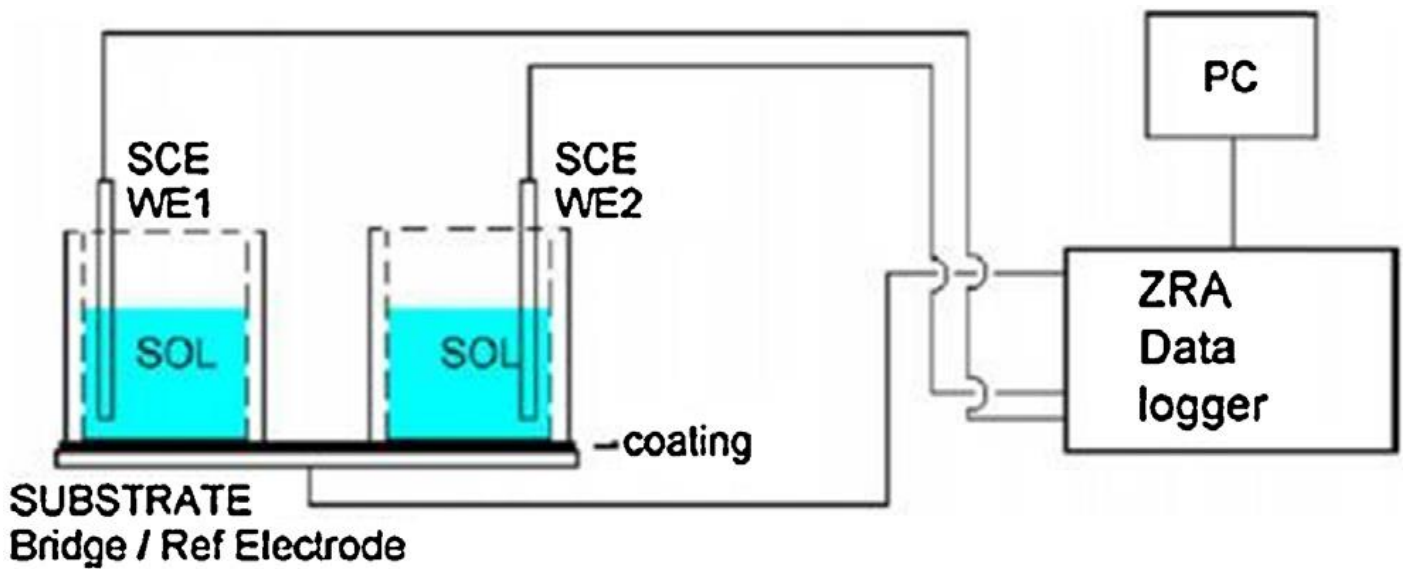


Figure 2-8: Single substrate arrangement for ENM (Mills *et al.*)

### 2.5.3 Direct current resistance

Mills and Mayne examined films by  $R_{DC}$ , dilatometry, and water absorption as a function of temperature. They were the first to observe the effects of film thermal transitions in electrochemical measurements. To measure  $R_{DC}$ , Granata and co-workers used two electrodes and an electrometer in the test cell. Because of the high resistance of the coatings, a high-impedance measuring instrument was required. A Keithley Model 610C electrometer capable of measuring resistance up to  $10^{14}$  ohm was used for DC measurement on the coatings. The instrument normally imposes a small known current, measures the voltage drop across the cell, and hence, allows  $R_{DC}$  to be calculated according to Ohm's law.  $R_{DC}$  of the test panel was measured using the test cell. In the case of in-situ measurements, the coated panel acted as one electrode and a reference (e.g. calomel or Ag-AgCl) as another electrode. The external current was so small that a separate CE was not required.  $R_{DC}$  measurement was performed by connecting the RE and the panel to the electrometer, after the panel surfaces had been exposed to the NaCl solutions at ambient temperatures. (Li *et al.*, 1998)

### 2.5.4 Gravimetric water uptake

Water diffusion through organic coatings can be monitored by the water absorption of the coating by the gravimetric method. Ca o-Paz, (2010) carried out gravimetric measurements for water-based styrene-acrylic latex paints to understand its correlation to the EIS method by immersing the samples in water for 15 days, which required a great amount of care and accuracy due to the small amount of water absorption. In fact, visible differences in weights are seen only at the third decimal place in the gram scale. The correlation between EIS and the gravimetry method was examined by plotting maximum water uptake observed against water absorption. All

the coatings exhibited a good linear correlation between the water uptake measured using EIS and the water absorption measured by the gravimetry method. Earlier, free films coupons were immersed in a 3wt% solution of NaCl. The initial weight and weight after immersion, were determined to an accuracy of  $\pm 0.1$  mg. Care was taken to complete the weighing within 2 m of taking the coupons out of the salt solution. Obviously, it was recognized that the differences in the water uptake was smaller than reported values. Also, even for thick films, saturation was reached within 48 h and water uptake after immersion at 90°C was definitely higher (estimated 2–3% wt) (Rouw, 1997).

Water uptake allows one to record the capacitance and mass data in real time. Moreover, plotting mass gain (or capacitance) versus the square root of time gives straight line behavior only at the very beginning of the experiment. Those visual observations indicate that the water uptake process is more complex than if it were purely diffusional. It appears that water can enter the coating without having a measurable effect on the capacitance of the coating. In addition, the role of fillers is found to be essential in the observed capacitive effect at long exposure times. It is suggested that fillers induce defects where water can accumulate (an increase in the pore tortuosity is included in this category) and/or they are of hydrophilic character (Cao-Paz, 2010).

### 3 Chapter 3: Scope and objectives

Polymer coatings are widely used for pipeline protection.  $T_g$  affects many properties of polymers including water sorption. The objective of this research is to provide a comprehensive view of the protection behavior for two polymers coatings, namely SP2888 and SP8888, in a temperature range around the transition temperature  $T_g$ , using EIS. To meet the objectives, the work was subdivided into the following tasks:

- Characterize the coatings morphologies and determine the  $T_g$ 's
- Conduct OCP and EIS tests on the samples at different temperatures over the selected range.
- Find the electrochemical equivalent circuit (EEC).
- Transform the frequency domain EIS data into a temperature domain diagram represented by  $Z_{\theta_{\min}}$ ,  $Z_{\theta_{\max}}$ ,  $Z_{10\text{Hz}}$ , and  $Z_{\theta=45}$ .
- Determine the weight fraction of the coatings as a function of temperature using gravimetric test.
- Conduct EN testing on the samples and determine  $R_n$ .

## **4 Chapter 4: Testing Materials and Experimental work**

### **4.1 Tested materials**

Two types of organic polymer coatings (SP2888 and SP8888) were provided by Specialty Polymer Coatings (SPC) in two forms:

Coated 30cm X 30cm carbon-steel (commonly used in oil and gas industry) substrates. These testing specimens were prepared by the supplier by sandblasting the substrates to achieve a roughness of more than 62.5  $\mu\text{m}$  that is suitable for applying the coating using a pressure spray technique at room temperature. The thickness of the coating was 0.5 mm. We used them for electrochemical tests (EIS and EN).

Free-standing films for each coating of 0.1 mm thickness were provided by the supplier too. The films were used in DSC and gravimetric tests

Both SP8888 and SP2888 are Fusion Bond Epoxy and Fiber-Reinforced Plastic coatings. Cab-O-Sil was used as the filler for both coatings. SP2888 contains Bisphenol A and Bisphenol F while SP8888 contains Anolac and  $\text{Fe}_2\text{O}_3$ .

#### **4.1.1 Testing cell**

EIS tests were conducted in a self-made three electrodes flat cell. It was put together by mounting an opening of glass cylinder (9 cm in diameter) directly on a coated specimen using silicon glue. Afterwards, suitable size lid with holes for the electrodes, was used to cover the upper opening of that cylinder as shown in fig. 4-1. A saturated calomel electrode (SCE) with a

potential of 0.242 V<sub>SHE</sub> was used as a reference while graphite rod was used as a counter electrode (CE). The working electrode (WE) was connected to the carbon-steel substrate.

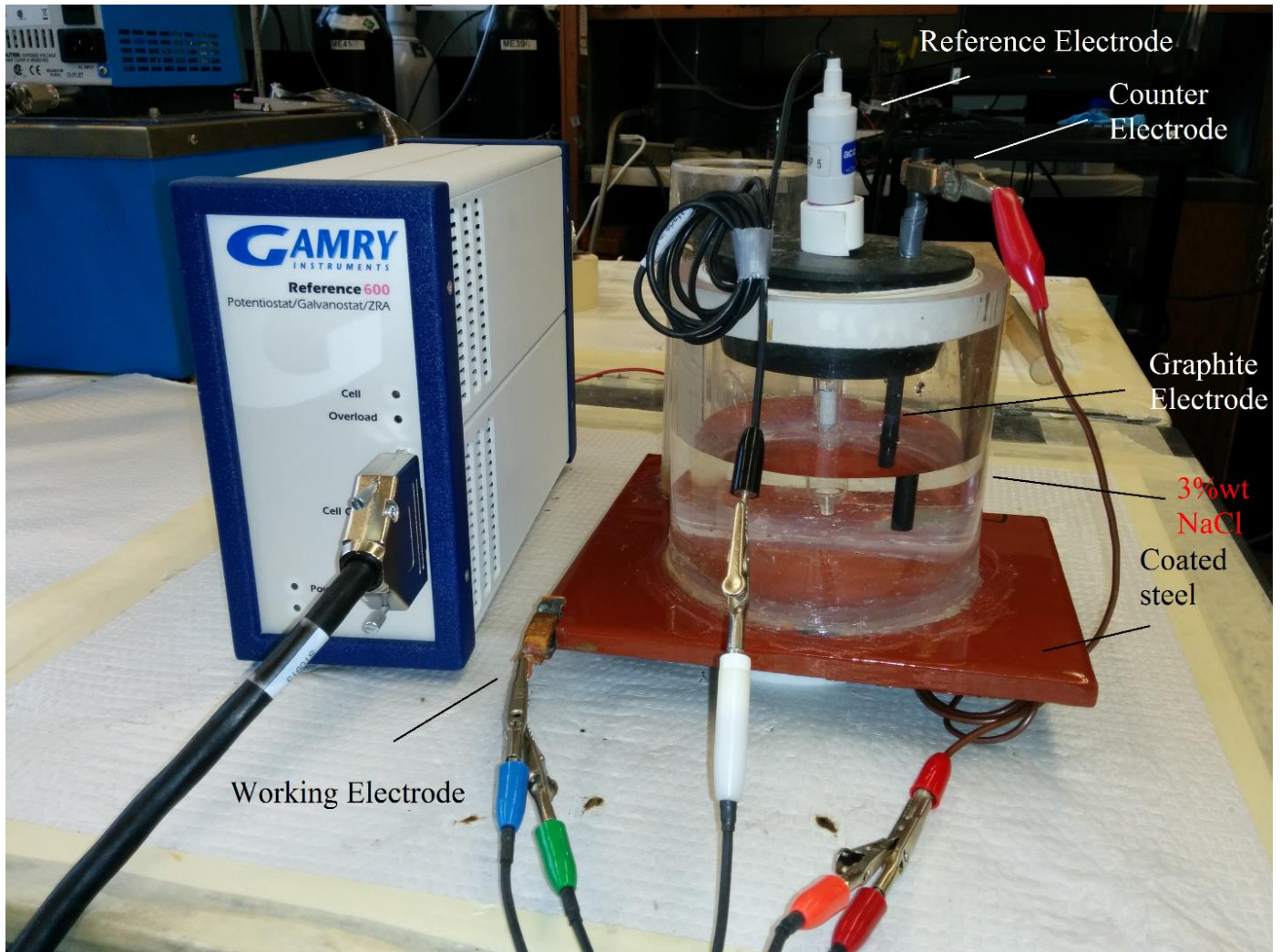


**Figure 4-1: EIS testing setup**

### **4.1.2 Electrolyte**

A 3%wt NaCl electrolyte is commonly used for coating testing (Oliveira and Ferreira, 2003; Szociński et al., 2010), it was used for all the electrochemical tests. The electrolyte solution was prepared by dissolving reagent-grade NaCl, (Fisher Scientific) in deionized water.

### **4.1.3 Faraday cage**

Running an open circuit potential test (OCP) or EIS on high impedance thick coatings such as SP2888 or SP8888 results in very rough measurements due to the insufficient current in the circuit. The current was low enough to be susceptible for electromagnetic interference from signals emitted from electric equipment in the lab. To avoid such noise, a Faraday cage was used to shield the experiment from external electromagnetic signals.

## **4.2 Characterization**

### **4.2.1 Differential Scanning Calorimetry (DSC)**

To prepare the samples, coatings were ground to small particles. 5-10 mg were used in DSC aluminum trays which were then compression sealed with aluminum lids. To ensure the safety of the DSC machine, one filled tray of each coating type was set in an oven at 200°C for one hour. Then, DSC test was performed on three testing samples from each coating type to ensure the reproducibility of the data. Using a TA Instrument Q1000, heat flow values were captured as a function of temperature, which was ramped from 20 to 200°C at 4°C/min.

#### **4.2.2 Energy-dispersive X-ray spectroscopy/ Scanning electron microscope (EDX/SEM)**

A small peel of the coatings was embedded in epoxy using a mold. Then, repeatedly polished and to achieve smooth surface. A 10 nm thick layer of 60:40 Gold and Palladium was applied on that surface to reduce surface charging. A Hitachi S-3000N scanning electron microscopy (SEM) with energy dispersive X-ray spectroscopy (EDX) was used in this test. The morphology of the coatings using different working distances, beam energies, and magnifications was examined using SEM in order to obtain high magnification images. Also, elemental distribution scans were done using the energy dispersive X-ray spectroscopy (EDX) to identify the composition of the coating surface.

#### **4.2.3 Gravimetric testing**

Three 1 x 1 cm coupons of free-standing coating from each type (SP2888 and SP8888) were weighted dry and after immersion for an hour in 3%w NaCl. Repeatedly, the coupons were dried off before measurements. The weight increase was marked as a solution intake at that temperature. Then, weight fraction was calculated by normalizing the solution intake values to the dry coating weight.

### **4.3 Electrochemical testing**

#### **4.3.1 Electrochemical impedance spectroscopy tests (EIS)**

An OCP followed by potentiostatic EIS tests was done on both coatings (SP2888 and SP8888) in the temperature range of 20 to 90°C. Using a Gamry Reference 600 potentiostat, the voltage applied for the tests consisted of -0.85 V<sub>SCE</sub> DC (to provide cathodic protection as was estimated

from Iron purbix diagram) and a perturbation voltage that was  $100\text{mV}_{\text{SCE}}$  for all the tests. The frequency range of the applied AC signal ranged from  $10^{-2}$  to  $10^4\text{Hz}$ .

#### **4.3.2 Electrochemical Noise tests (EN)**

Similar to EIS, EN was performed on the coatings SP2888 and SP8888 at temperature range of  $20\text{--}80^\circ\text{C}$  in a 3%wt sodium chloride solution. A single substrate setup, as shown in figure 2-8, was used to measure the potential and current in a ZRA mode using the potentiostat. The measurements were run for 180s at each interval. Six intervals were captured at each temperature point.

## 5 Chapter 5: Results and Discussion

### 5.1 Coating characterization

#### 5.1.1 Differential scanning calorimetry (DSC)

When a thermoplastic material gets heated to a temperature reaching the start of the transition band, an energy flow (heat) will be required in the transition to breakdown the side chains. This energy flow can be an indicator for identifying  $T_g$ . To identify the  $T_g$  of each coating, heat flow and reversing heat flow were measured as a function of temperature, which was ramped from 20 to 200°C at 4°C/min and graphically reported. On the graph as shown in figure 5.1 and 5.2, the first sharp increase in slope (in the expected occurrence region of  $T_g$ ) was observed to extrapolate the  $T_g$  value.

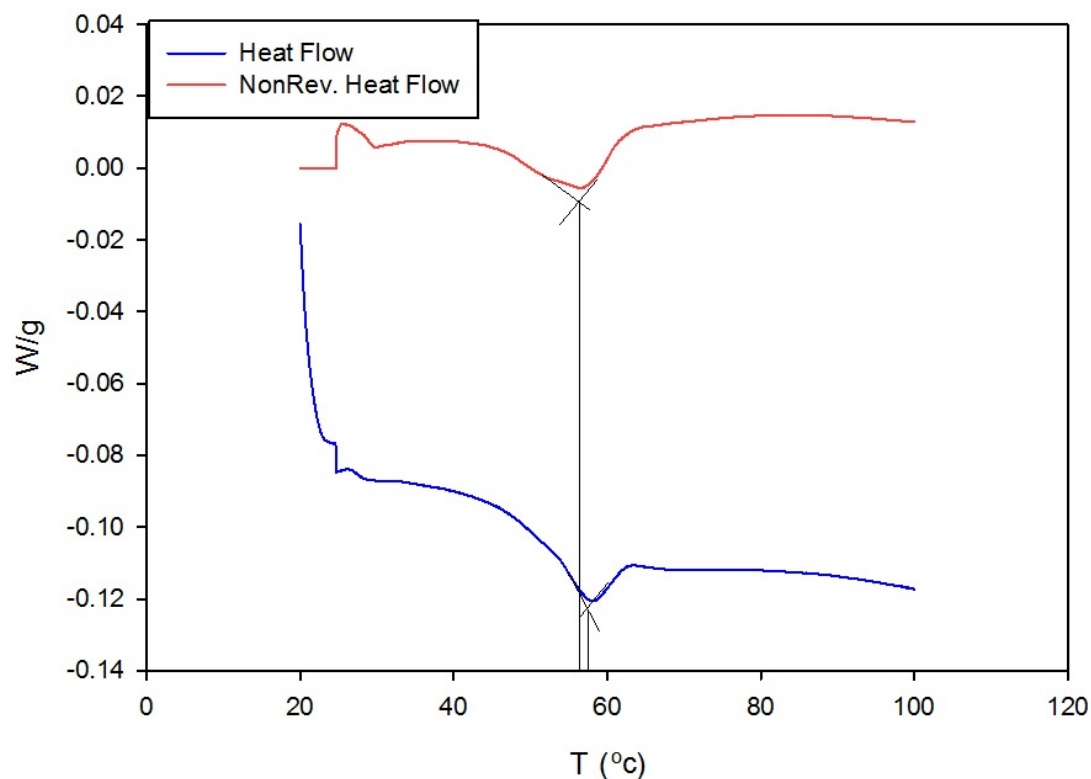


**Figure 5-1: Heat flow and non-reversing heat flow vs T (°C) from DSC for SP2888.**

Figures 5.1 and 5.2 respectively show one of the three results of the heat flow and the reversing heat flow from DSC experiments that were performed on the coatings for SP2888 and SP8888 to obtain their  $T_g$  values. Table 5-1 shows all the results at the three runs. The average of the  $T_g$  transition values for SP2888 coating occurred at  $58.3 \pm 0.6^\circ\text{C}$  while the average for SP8888 coating occurred at about  $63.7 \pm 0.5^\circ\text{C}$ . Thus, the temperature range (from 20 to  $80^\circ\text{C}$ ) was seemed to be suitable for this study.

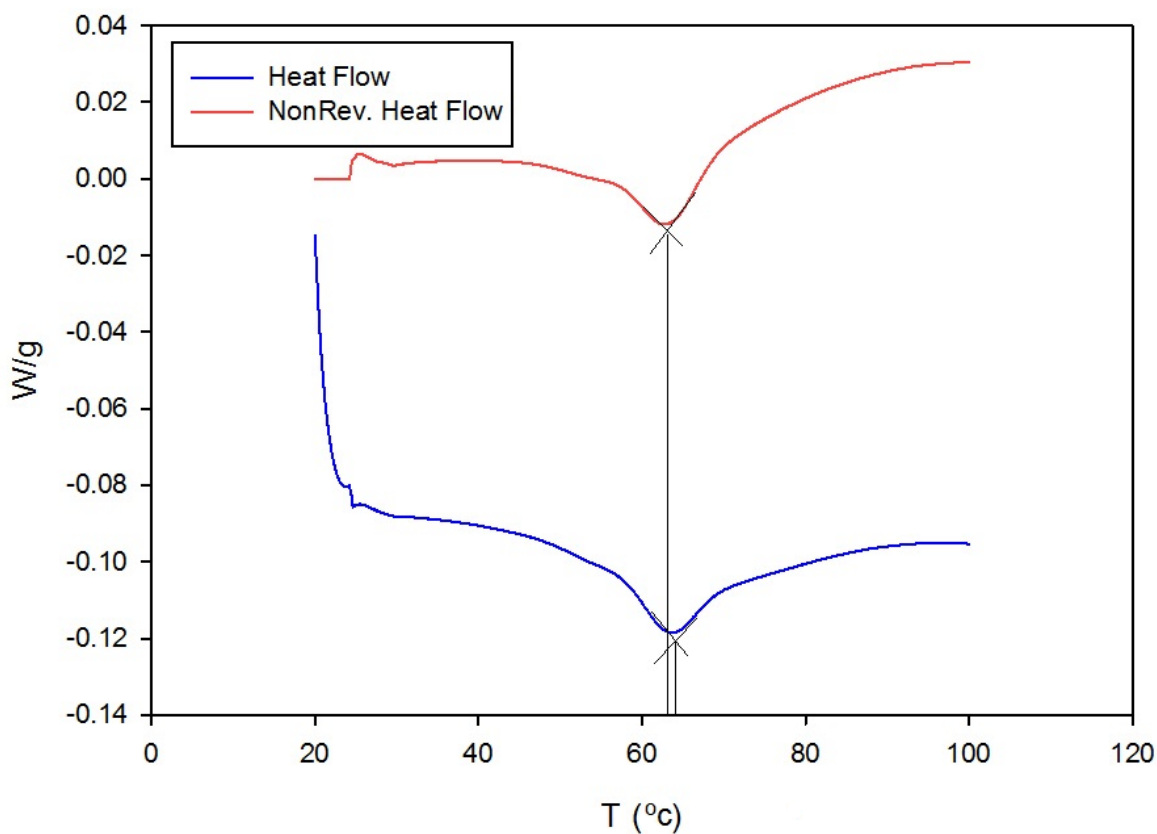


**Figure 5-2: Heat flow and non-reversing heat flow vs T (°C) from DSC for SP8888.**

**Table 5-1: T<sub>g</sub> from Heat flow and non-reversing heat flow**

|        |      | T <sub>g</sub> non-rev heat<br>flow (°C) | T <sub>g</sub> heat flow<br>(°C) | Average T <sub>g</sub> (°C) |
|--------|------|--|----------------------------------|-----------------------------|
| SP2888 | Run1 | 58.44                                    | 58.24                            | 58.3 ± 0.64                 |
|        | Run2 | 57                                       | 58.4                             |                             |
|        | Run3 | 58.9                                     | 58.9                             |                             |
| SP8888 | Run1 | 63.62                                    | 64.49                            | 63.7 ± 0.5                  |
|        | Run2 | 62.92                                    | 63.46                            |                             |
|        | Run3 | 63.63                                    | 64.16                            |                             |

**5.1.2 Morphologies**

To characterize the surface morphology of untested coatings, OLM, SEM, and EDX techniques were utilized. Images from OLM and SEM showed that both coatings have smooth surfaces with some randomly appeared blisters of different diameters as shown in figures 5-3 and 5-4. With higher magnification, these blisters were observed to have a smooth surface at the bottom with some smaller blisters and grooves as shown in figures 5-5 and 5-6. These little blisters could be an end of deep micro pathways. Interestingly, the EDX of the blister showed less abundance of NaCl and more Al than the rest of the surface, as shown in figure 5-7. Generally, metal fillings are commonly used in polymer coatings, but its excess might be related to the reason of blistering.

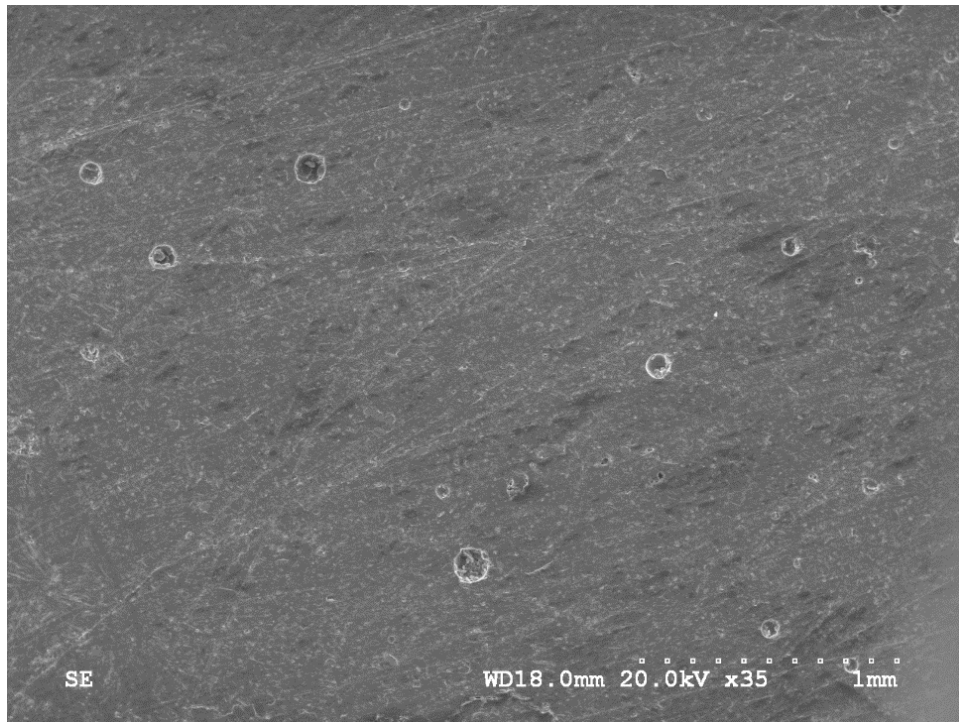


**Figure 5-3: SEM image for SP2888**

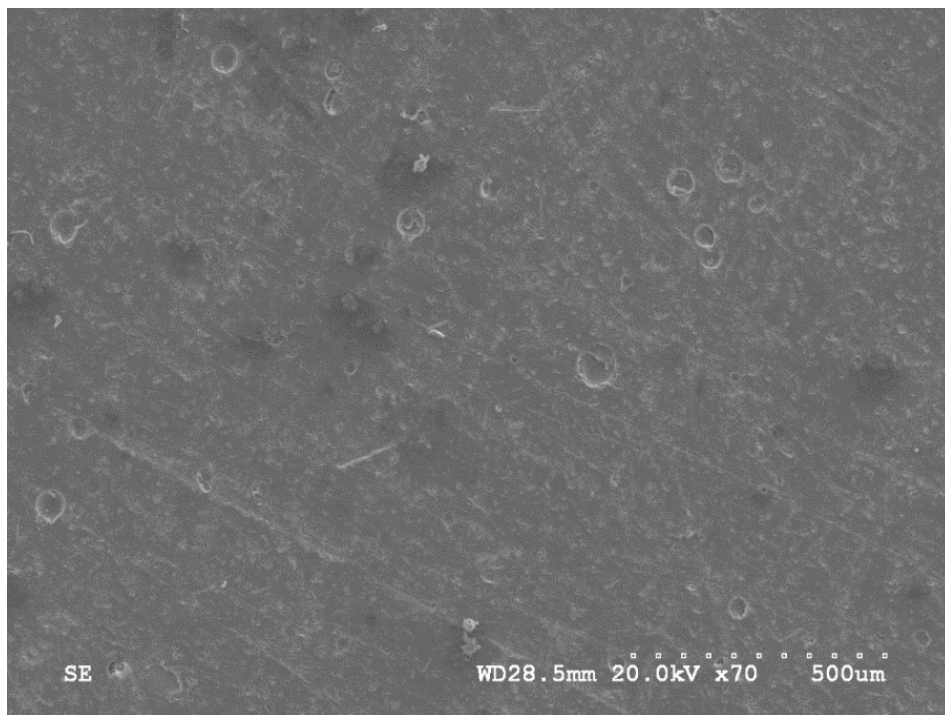


**Figure 5-4: SEM image for SP8888**

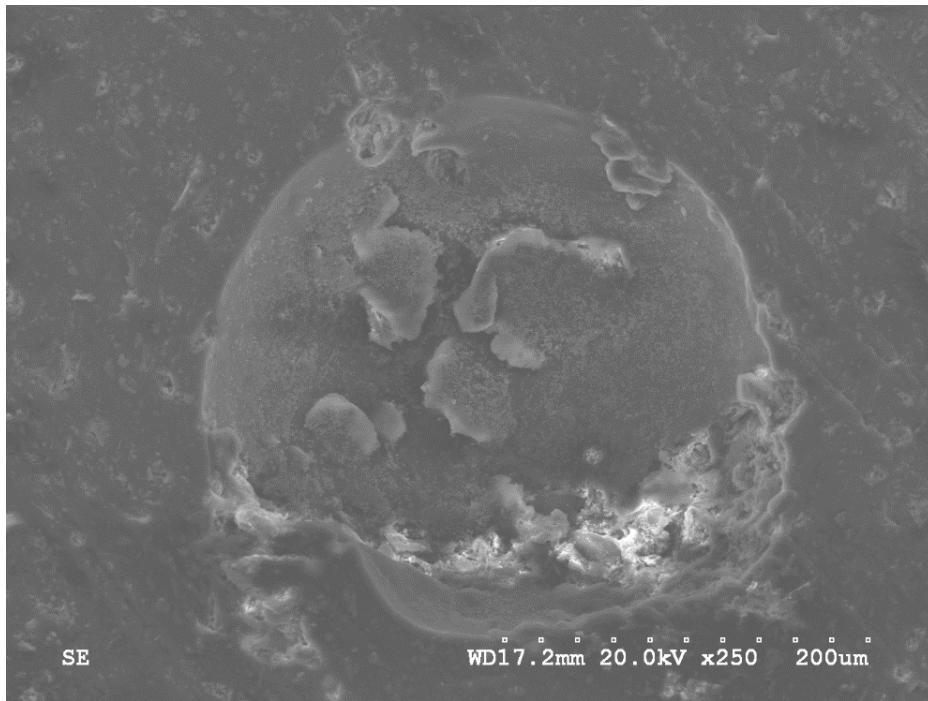


**Figure 5-5: SEM image for SP2888 coating pore in with 250X magnification**

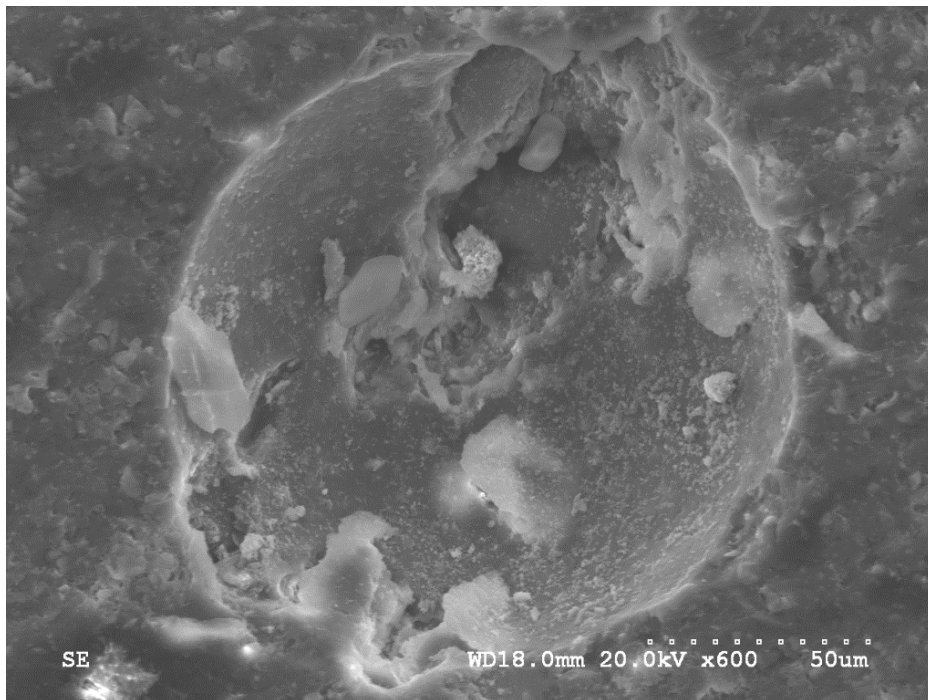


**Figure 5-6: SEM image for SP8888 coating pore with 250X magnification**

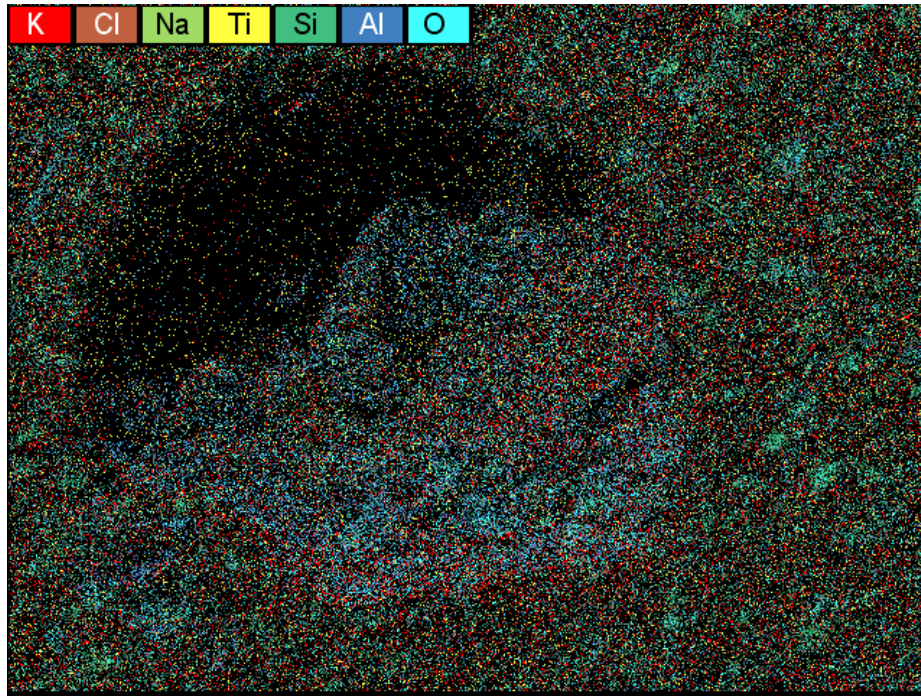


**Figure 5-7: Mapping EDX for SP2888**

### **5.1.3 Gravimetric test**

The measured weights were recorded after each immersion in a different temperature until all the test range was covered. All the measurements were then normalized to the sample dry weight and plotted versus temperature, as shown in figure 5-8.

From the figure, the weight fraction increased as the temperature increased which indicates water uptake. Both samples (SP2888 and SP8888) exhibit similar slope, but SP2888 had more weight fraction and more deviation between the three sample measurements. However, there was no evidence of transition temperature effect on the water intake that can be recognized from the plot.

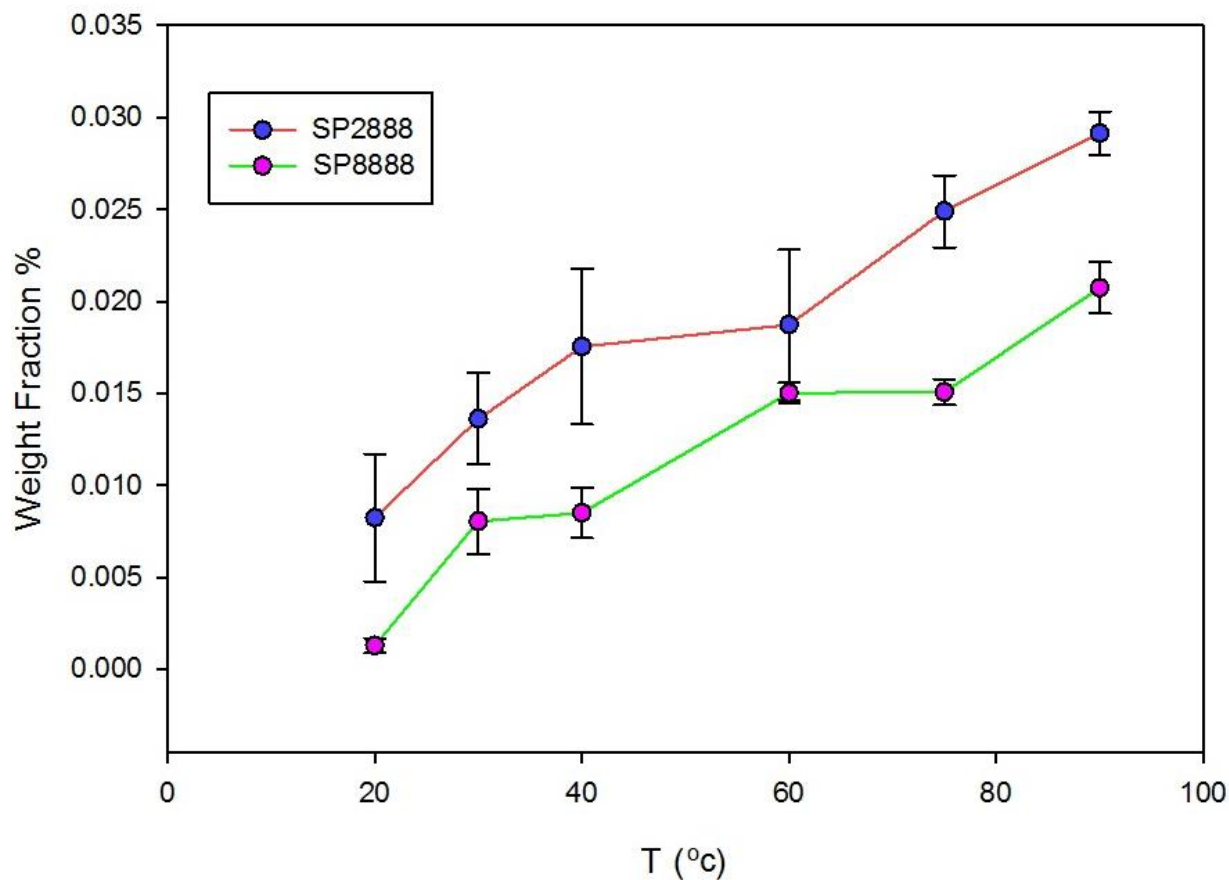


**Figure 5-8: Measured gravimetric water weight fraction for SP8888 and SP2888 in 3% wt NaCl at different temperatures.**

## 5.2 Electrochemical testing

In this section, electrochemical testing techniques have been used to study the corrosion protection performance of the samples at a temperature range of 20–80°C. This range of temperatures was chosen to include the transition temperature for both samples.

### 5.2.1 Electrochemical Impedance Spectroscopy (EIS)

To measure the impedance of SP2888 and SP8888 coatings in 3%wt sodium chloride electrolyte and temperature range of 20 to 80°C, an EIS technique was employed. The EIS was performed

repeatedly to insure the reproducibility of the results, as shown in figures 5-9 and 5-12 for SP2888 and SP8888, respectively. The measured impedance and phase (Bode plot) for coating SP2888 are shown in figures 5-10 and 5-11 respectively, these results show a drastic drop in impedance as the temperature increased from 20 to 80°C 3 on the log scale. On the other hand, the phase has drastically changed from capacitive to resistive behavior. Less intensively, the change occurred with the impedance of SP8888 over the same temperature change (1.5 on the log scale) as shown in figure 5-13, but the phase has shown more aggressive change toward resistive behavior as shown in figure 5-14.

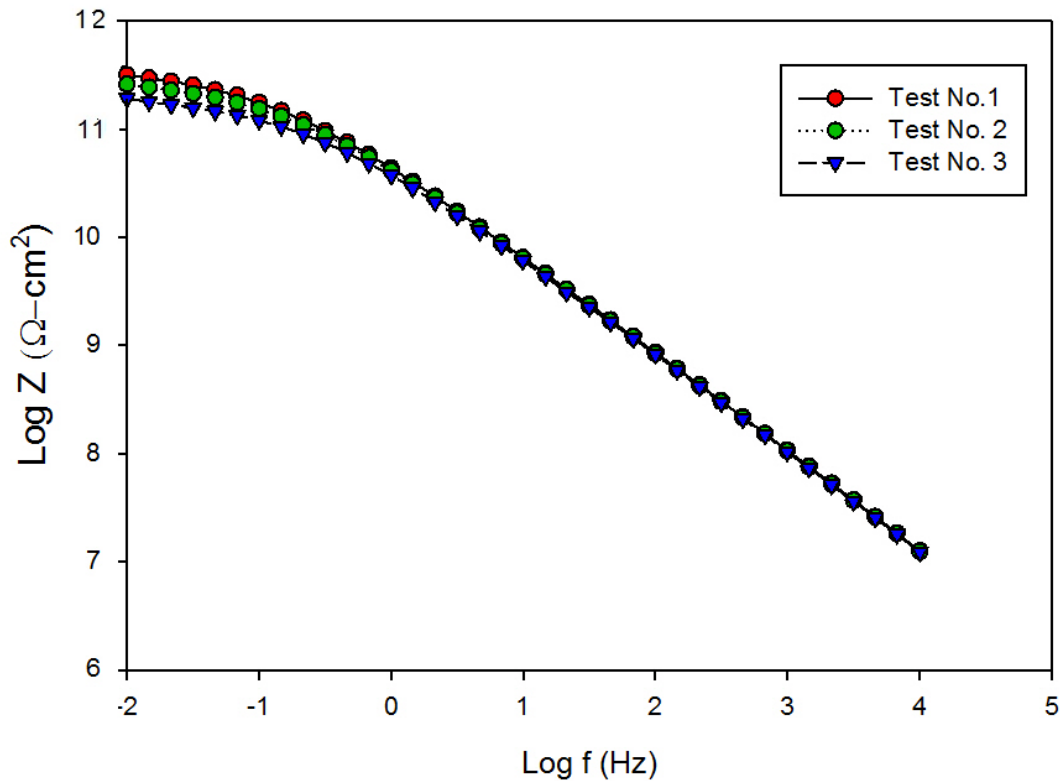


**Figure 5-9: Impedance from 3 EIS tests, for coating SP2888 in 3%wt NaCl at 30°C**

Li *et al.* (1998) found that the impedance modulus leveled off at the low-frequency end to lower values as the temperature increased. At higher frequencies, temperature effects disappeared, and

the curves overlapped. Also, the impedance modulus has drastically dropped from 10 to 6 (on the log scale) at low frequencies. This impedance drop increases the chances of corrosive agents to go through the coating. Even though impedance is an important factor to evaluate the protection performance of coatings, the concern in this work is more about its change with temperature than the impedance itself. Thus, to examine the behavior of the impedance modulus in terms of temperature, the EIS data was reconstructed in temperature domain as will be illustrated later.

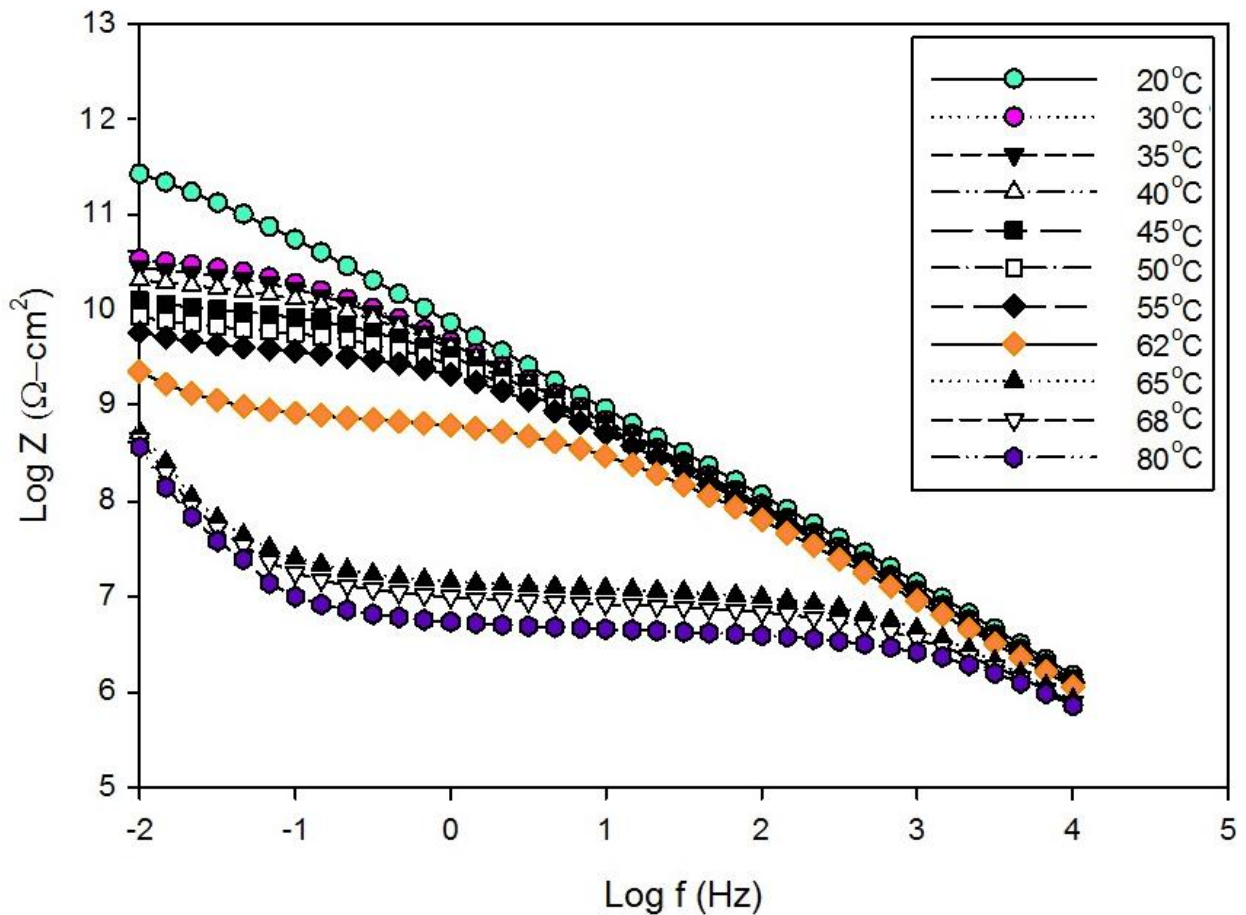


**Figure 5-10: Impedance modulus for coating SP2888 in 3%wt NaCl**

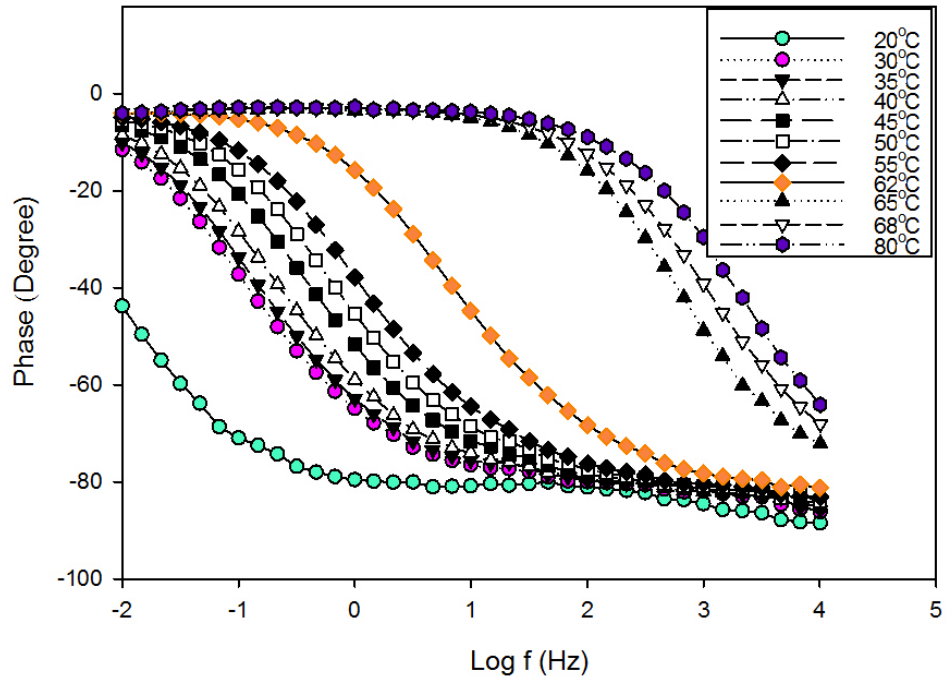


**Figure 5-11: Impedance phase for SP2888 coating in 3%wt NaCl**

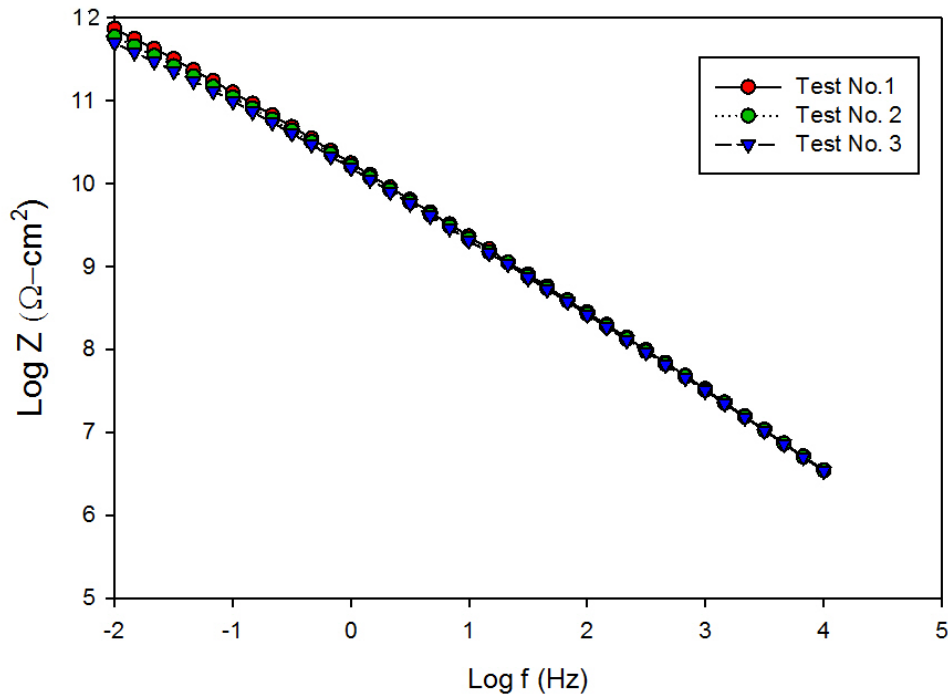


**Figure 5-12: Impedance from 3 EIS tests, for Coating SP8888 in 3%wt NaCl at 30 C°**

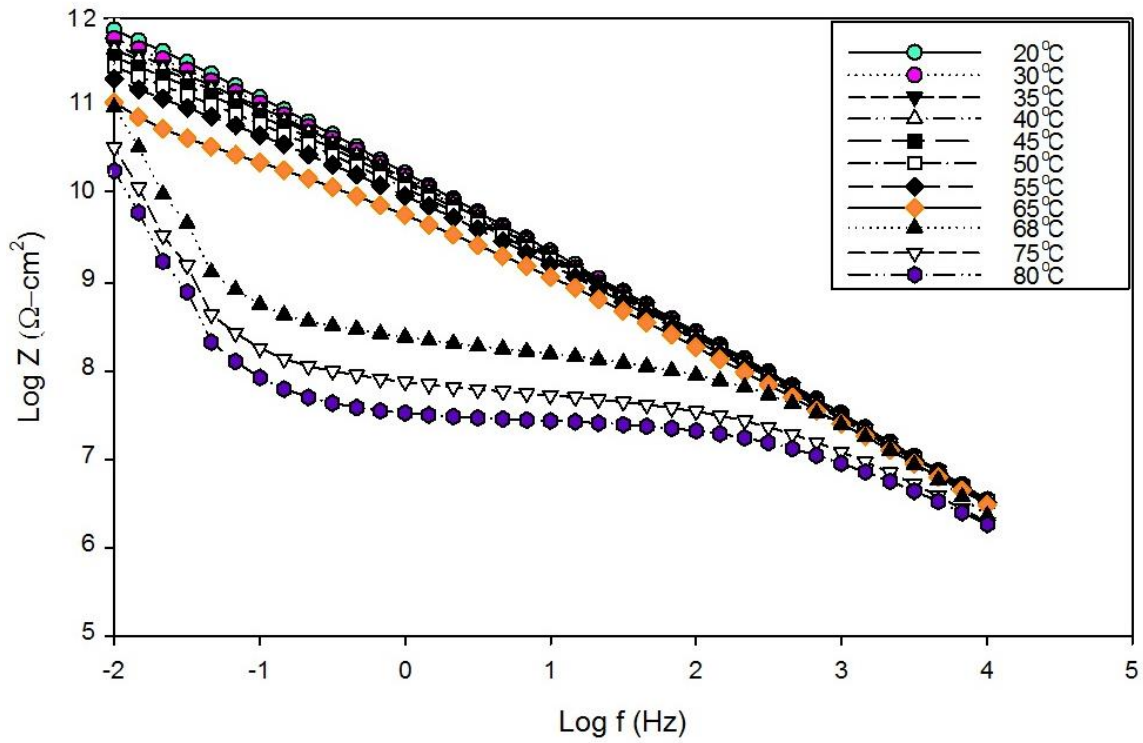


Figure 5-13: Impedance modulus for SP8888 coating in 3%wt NaCl

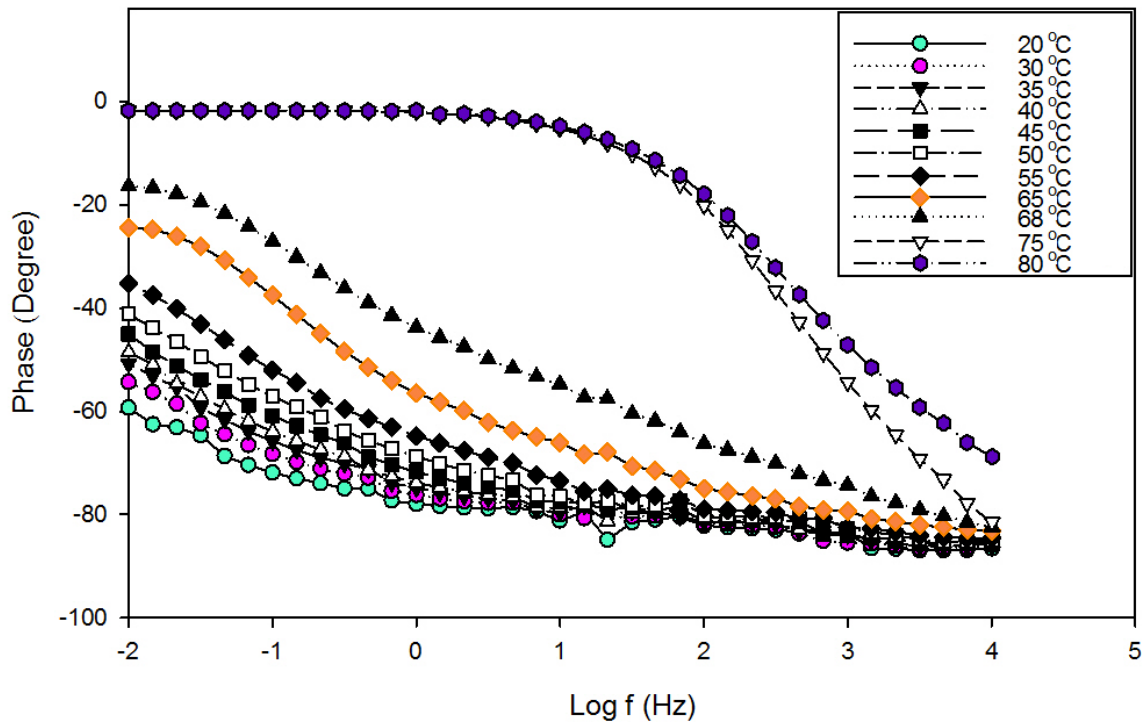
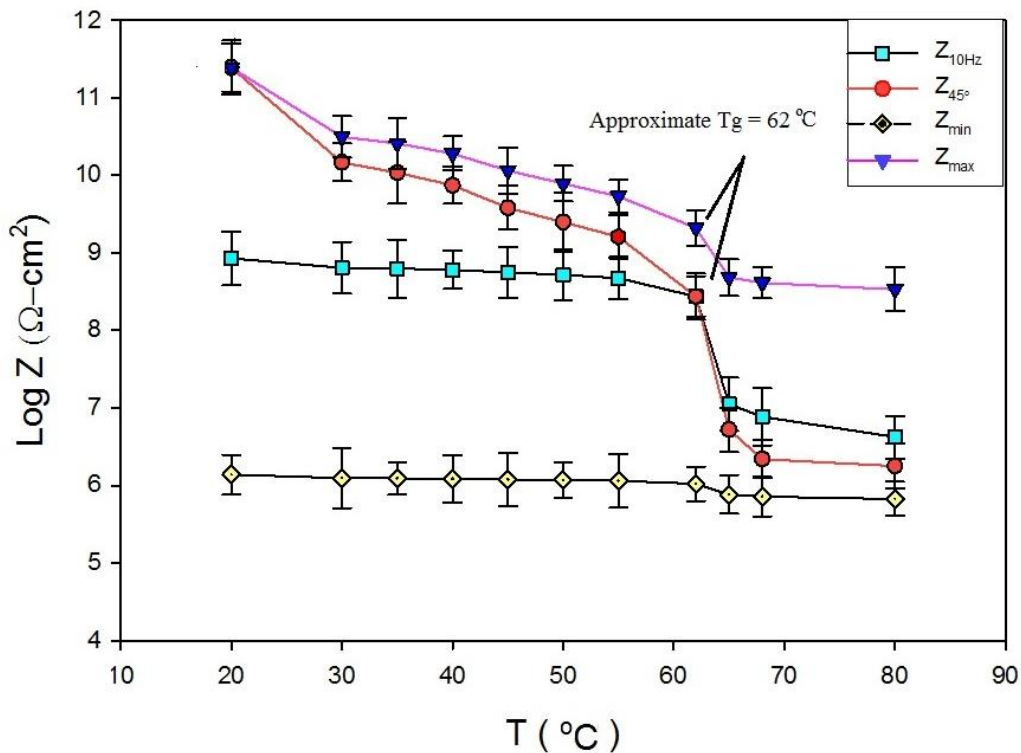
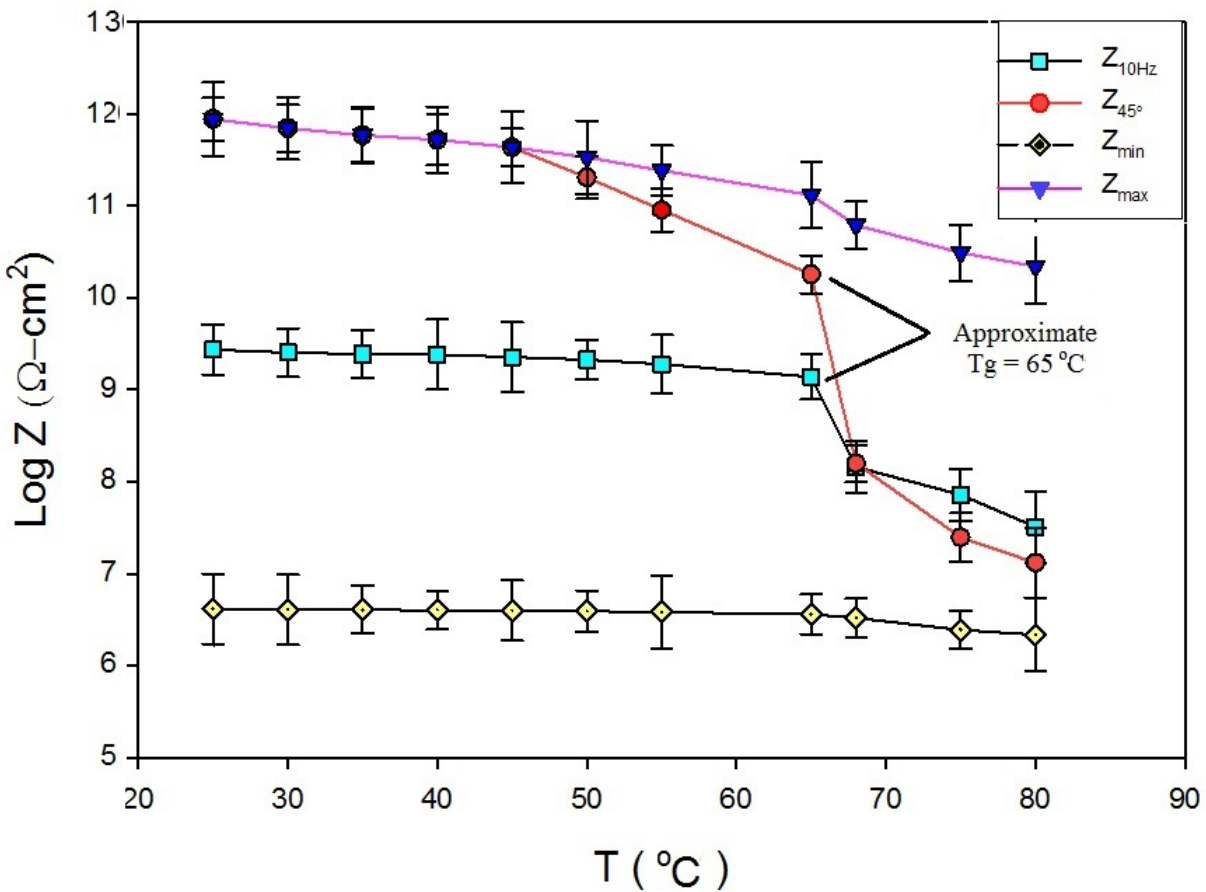


Figure 5-14: Impedance phase for SP8888 coating in 3%wt NaCl

As mentioned earlier, AC measurements in EIS tests were performed at a frequency range from  $10^{-2}$  to  $10^4$  Hz which will result in frequency spectra with many frequencies that could be used to represent the impedance of the coating. In literature, the four methods used are  $Z_{f \text{ min}}$ ,  $Z_{f \text{ max}}$ ,  $Z_{\theta=45}$ , and  $Z_{10\text{Hz}}$ . With each method, the impedance values for SP2888 and SP8888 were plotted versus the temperature of measurement as shown in figures 5-15 and 5-16. Generally, the impedance representations were linear in some intervals, which indicate an energy dependence and can be described as Arrhenius-type systems. Nevertheless, the slope of  $Z_{\text{min}}$  was almost constant, so it was not sensitive enough to reflect the temperature effects. On the other hand,  $Z_{\text{max}}$ ,  $Z_{\theta=45}$ , and  $Z_{10\text{Hz}}$  decreased with increasing temperature.  $Z_{\text{max}}$  was, comparatively, the highest value at all temperatures for both samples, but was not as sensitive to the temperature changes as  $Z_{\theta=45}$ , and  $Z_{10\text{Hz}}$  were.  $Z_{\theta=45}$ , and  $Z_{10\text{Hz}}$  showed abrupt changes in slope at some temperature points. Most obviously at  $62^\circ\text{C}$  for SP2888 and  $65^\circ\text{C}$  for SP8888.



**Figure 5-15:  $Z_{\text{min}}$ ,  $Z_{\text{max}}$ ,  $Z_{\theta=45}$ , and  $Z_{f=10 \text{ Hz}}$  for SP2888 in 3% wt NaCl**



**Figure 5-16:  $Z_{min}$ ,  $Z_{max}$ ,  $Z_{\theta=45}$ , and  $Z_{f=10\text{ Hz}}$  for SP8888 in 3%wt NaCl**

To further analyze the results, an electrical equivalent circuit technique was employed to characterize the coatings at each temperature under tests based on the EIS results. Figure 5-17 shows the model used and figure 5-18 shows the physical representation of that model. Using the Gamry Echem Analyst software, a fit was performed where a simplex algorithm was used to calculate values of the model elements that score minimum value of goodness of fit. It was possible to develop an electric circuit model, as shown in figure 5-17, that represents both systems.

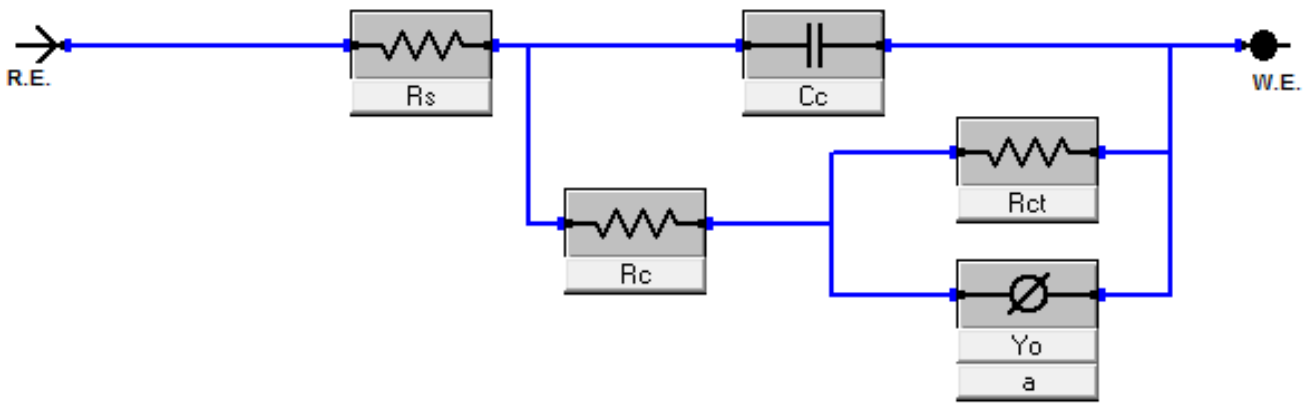


Figure 5-17: EEC used to represent coatings SP8888 and SP2888

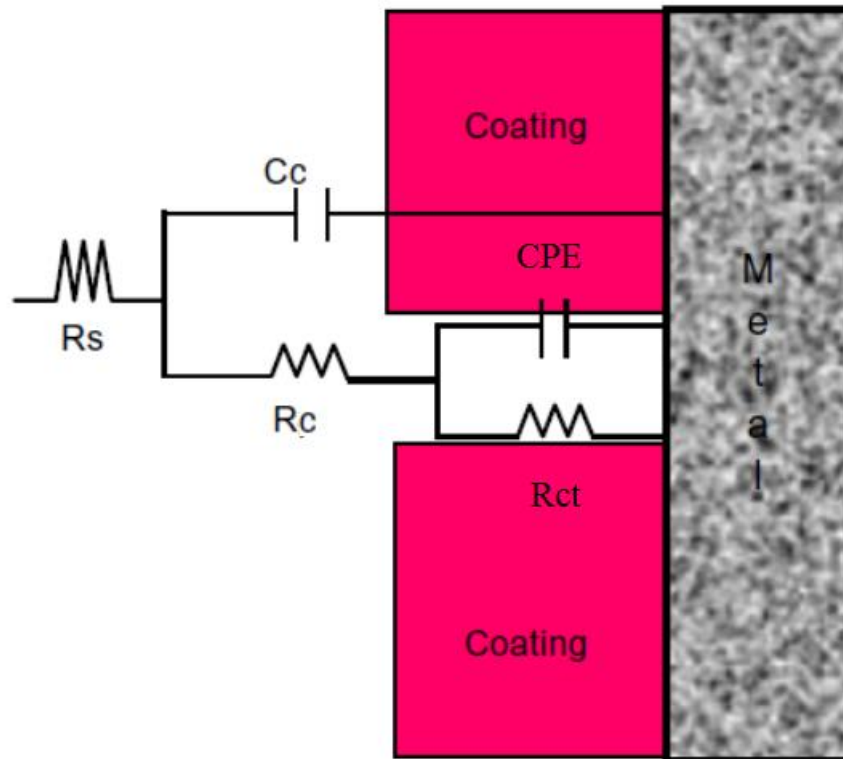


Figure 5-18: physical representation of the EEC used to represent the coating systems

In figure 5-17,  $R_s$  represents electrolyte resistance,  $C_c$  and  $R_c$  represent coating capacitance and resistance respectively, and  $R_{ct}$  and CPE represent charge transfer resistance and the phase that occurred due that transfer. The values for  $R_s$ ,  $R_c$ ,  $R_{ct}$ , and  $C_c$  for both coatings are presented in tables 5-2 and 5-3.

**Table 5-2: Calculated EEC elements' values for SP2888 at different temperatures**

| Element/<br>T(C°) | 45       | 50       | 55       | 62       | 65       | 68       | 80       | Units                 |
|-------------------|----------|----------|----------|----------|----------|----------|----------|-----------------------|
| <b>Rc</b>         | 6.89E+06 | 5.93E+06 | 2.51E+06 | 1.58E+06 | 1.02E+06 | 4.46E+03 | 4.31E+03 | Ohm-cm <sup>2</sup>   |
| <b>Cc</b>         | 1.25E-11 | 1.28E-11 | 1.35E-11 | 1.52E-11 | 2.12E-11 | 2.10E-11 | 2.10E-11 | F/ cm <sup>2</sup>    |
| <b>Rct</b>        | 1.06E+10 | 6.81E+09 | 4.31E+09 | 9.89E+08 | 6.16E+08 | 6.66E+08 | 4.23E+09 | Ohm- cm <sup>2</sup>  |
| <b>Rs</b>         | 2.99E-01 | 2.04E-01 | 1.45E-01 | 1.33E-01 | 1.12E-01 | 9.47E-02 | 3.84E-02 | Ohm- cm <sup>2</sup>  |
| <b>Yo</b>         | 5.95E-11 | 7.09E-11 | 8.96E-11 | 2.88E-10 | 5.27E-08 | 3.79E-08 | 1.42E-07 | Ss^a/ cm <sup>2</sup> |
| <b>a</b>          | 6.88E-01 | 6.71E-01 | 6.52E-01 | 5.10E-01 | 1.38E-01 | 4.85E-01 | 1.09E-01 |                       |

**Table 5-3: calculated EEC element values for SP8888 at different temperatures**

| Element/<br>T(C°) | 40       | 45       | 50       | 55       | 65       | 80       | Units                 |
|-------------------|----------|----------|----------|----------|----------|----------|-----------------------|
| <b>Rc</b>         | 5.12E+07 | 5.11E+07 | 5.25E+07 | 3.23E+07 | 1.43E+07 | 7.61E+04 | Ohm-cm <sup>2</sup>   |
| <b>Cc</b>         | 3.37E-12 | 3.55E-12 | 3.51E-12 | 3.54E-12 | 3.68E-12 | 6.53E-12 | F/ cm <sup>2</sup>    |
| <b>Rct</b>        | 1.37E+12 | 1.49E+12 | 6.90E+11 | 3.52E+11 | 1.24E+11 | 1.17E+08 | Ohm- cm <sup>2</sup>  |
| <b>Rs</b>         | 8.26E-01 | 7.04E-01 | 6.30E-01 | 5.29E-01 | 4.11E-01 | 3.64E-01 | Ohm- cm <sup>2</sup>  |
| <b>Yo</b>         | 8.58E-12 | 1.03E-11 | 1.24E-11 | 1.66E-11 | 3.22E-11 | 8.01E-09 | Ss^a/ cm <sup>2</sup> |
| <b>a</b>          | 7.18E-01 | 6.87E-01 | 6.86E-01 | 6.73E-01 | 6.31E-01 | 2.05E-01 |                       |

From tables 5-2 and 5-3,  $R_c$  showed a decrease for both coatings as temperature increases. At 65°C,  $R_{ct}$  for SP2888 decreased from  $10^6$  to  $10^3$  ( $\Omega\text{-cm}^2$ ), and SP8888 decreased from  $10^7$  to  $10^4$  ( $\Omega\text{-cm}^2$ ). The coating capacitance showed a slight increase with temperature. Water ingress into coating pathways may be the reason for that increase. The BK equation (Eq. 2.22) is often used to calculate the volume fraction of water uptake using the coating capacitance change (Nguyen, 2005). A volume fraction for coatings SP2888 and SP8888 were calculated and plotted versus temperature of immersion and are shown in figures 5-23 and 5-24.

$R_{ct}$  is shown to be the dominant resistance.  $R_{ct}$  at 20°C is on the order of  $10^{10}$  and  $10^{12}$  ( $\Omega\text{-cm}^2$ ) for SP2888 and SP8888, then dropped as the temperature increased to 80°C to become  $10^9$  and  $10^8$

( $\Omega\text{-cm}^2$ ) respectively. However  $R_{ct}$  did not show much change around  $T_g$ .  $R_s$  was locked to a value less than  $1 \Omega\text{-cm}^2$  during iteration, which is the typical value for 3% wt NaCl solution.  $Y_0$  showed an increase from -11 to -7 and from -12 to -9 ( $Ss^a/ \text{cm}^2$ ) on the log scale for SP2888 and SP8888 respectively.

The goodness of fit was very low at temperatures below  $T_g$ , as shown in figures 5-19 and 5-21 for SP2888 and SP8888 respectively, which supports that the EEC model and the estimated values of elements are suitable to represent the coatings in that temperature range. However, above  $T_g$  the goodness of fit went to (0.12) for SP2888 and (0.16) for SP8888 as shown in figures 5-19 and 5-21, which indicates that EEC is not suitable to represent the coatings anymore. This can be only possible if a drastic change, from an electrochemical perspective, occurred on that coating. Logically, the only elements in the model that should be influenced are those representing the affected physical segments of the coating. By looking into the error, two elements are associated with high error values as the temperature approaches  $T_g$  and that error rapidly escalates thereafter,  $R_{ct}$  and CPE as can be seen in figure 5-20 and 5-22.  $R_{ct}$  has the highest error ratio in this temperature range and so the charge transfer could possibly be the most affected segment in the coating system. Apparently, the decrease  $R_{ct}$  exhibited around  $T_g$  for SP8888 (from 11 to 8 on the log scale) has shrunk the shift from the actual value (error ratio is 0.35) more than SP2888 which didn't exhibit any decrease (error ratio is 4). This pattern indicates that the actual value of  $R_{ct}$  has significantly dropped above  $T_g$ .

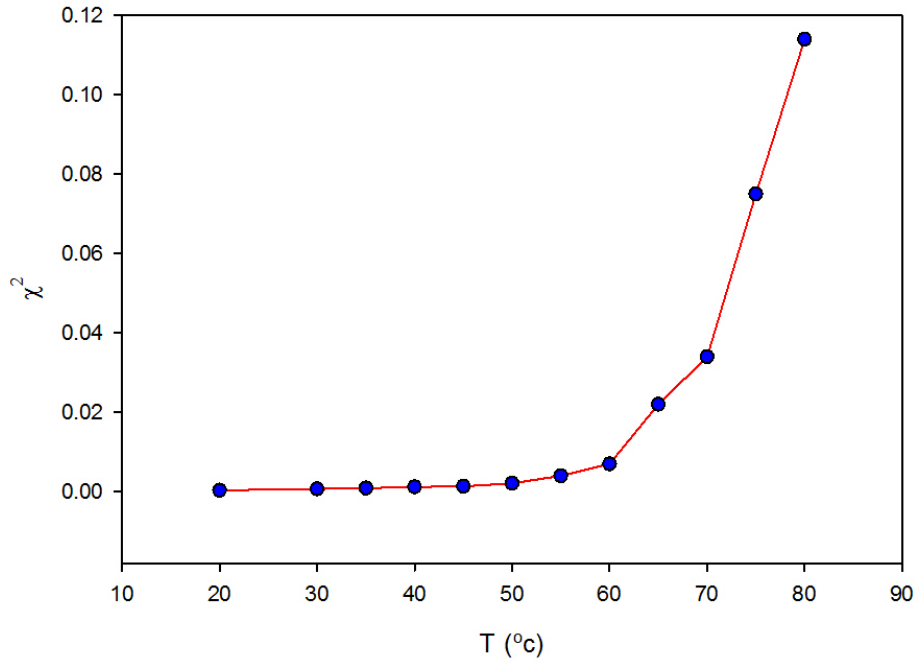


**Figure 5-19: Goodness of Fit vs T (°C) for SP2888 in 3%wt NaCl**

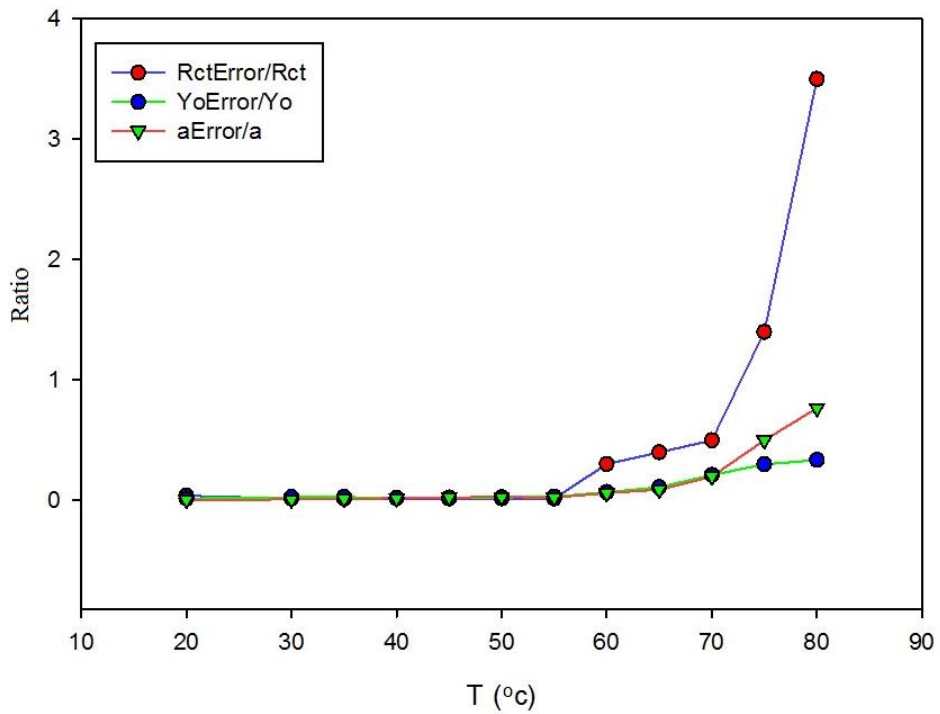


**Figure 5-20: The ratio of error arose in the value of calculated Rct and CPE parameters vs temperature for SP2888**

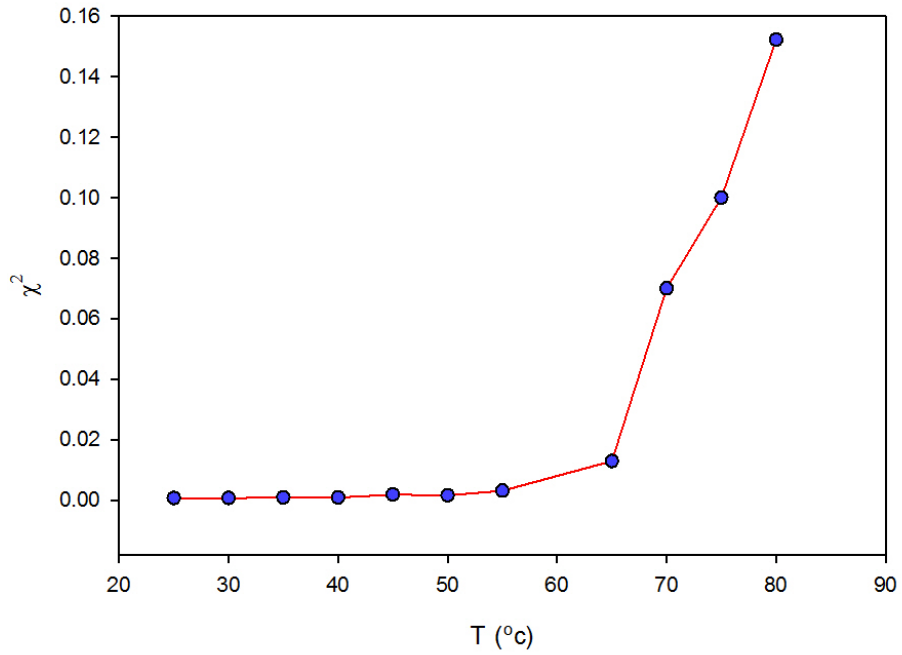


**Figure: 5-21: Goodness of Fit vs T (°C) for SP8888 in 3%wt NaCl**

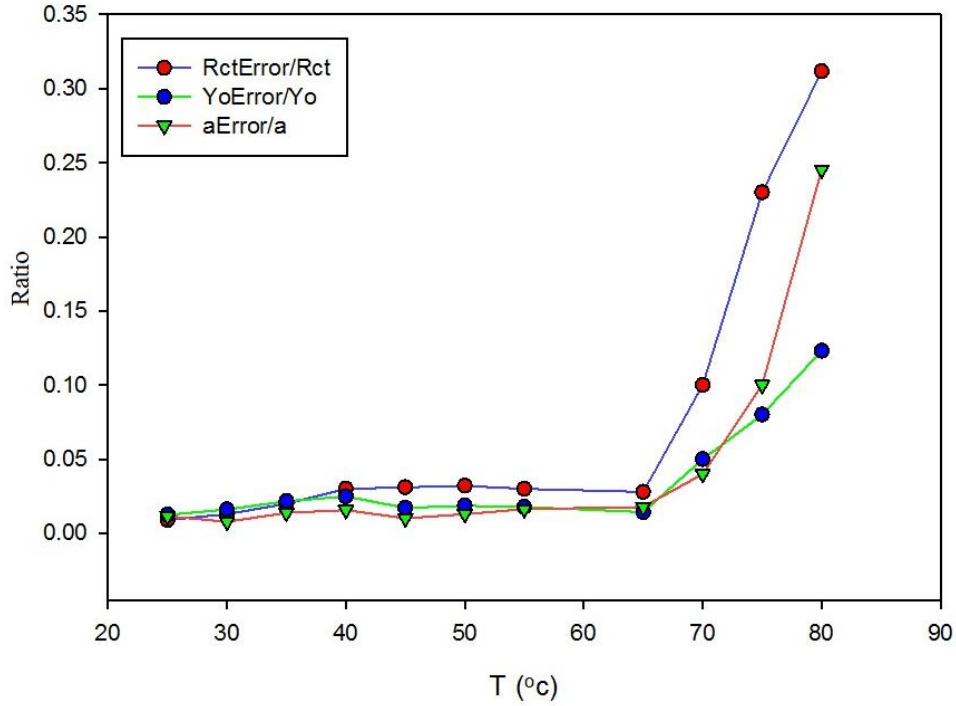


**Figure 5-22: the ratio of error arose in the value of calculated Rct and CPE parameters vs temperature for SP8888**

The calculated water volume fraction based on Cc change from EEC for both coatings, increased as the temperature was increased. An increase of water sorption as the temperature increases has been reported in many earlier works (Rezaei *et al.*, 2010b). The volume fraction values for both coatings were small compared to reported values for some other organic coatings, but yet the coatings exhibited a sharp slope change at 58°C and 60°C for SP2888 and SP8888 respectively.

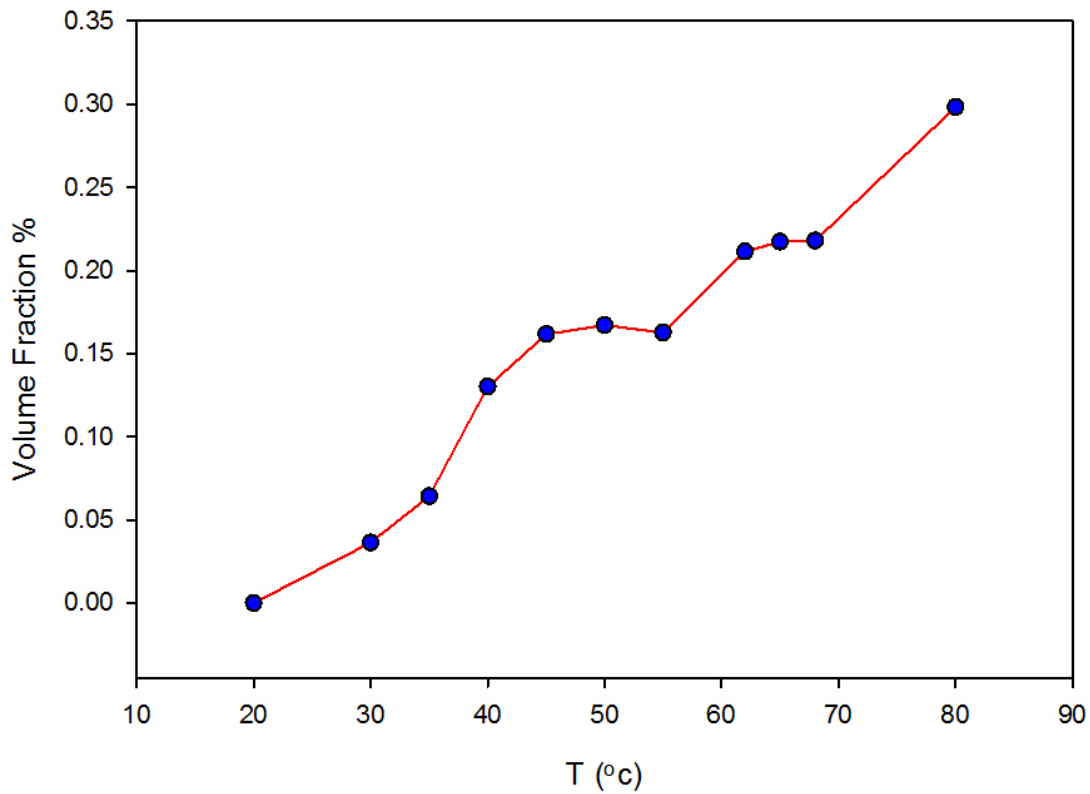


**Figure 5-23: Calculated volume fraction change due temperature for SP2888 in 3%wt NaCl based on the change in value of coating capacitance (Cc)**

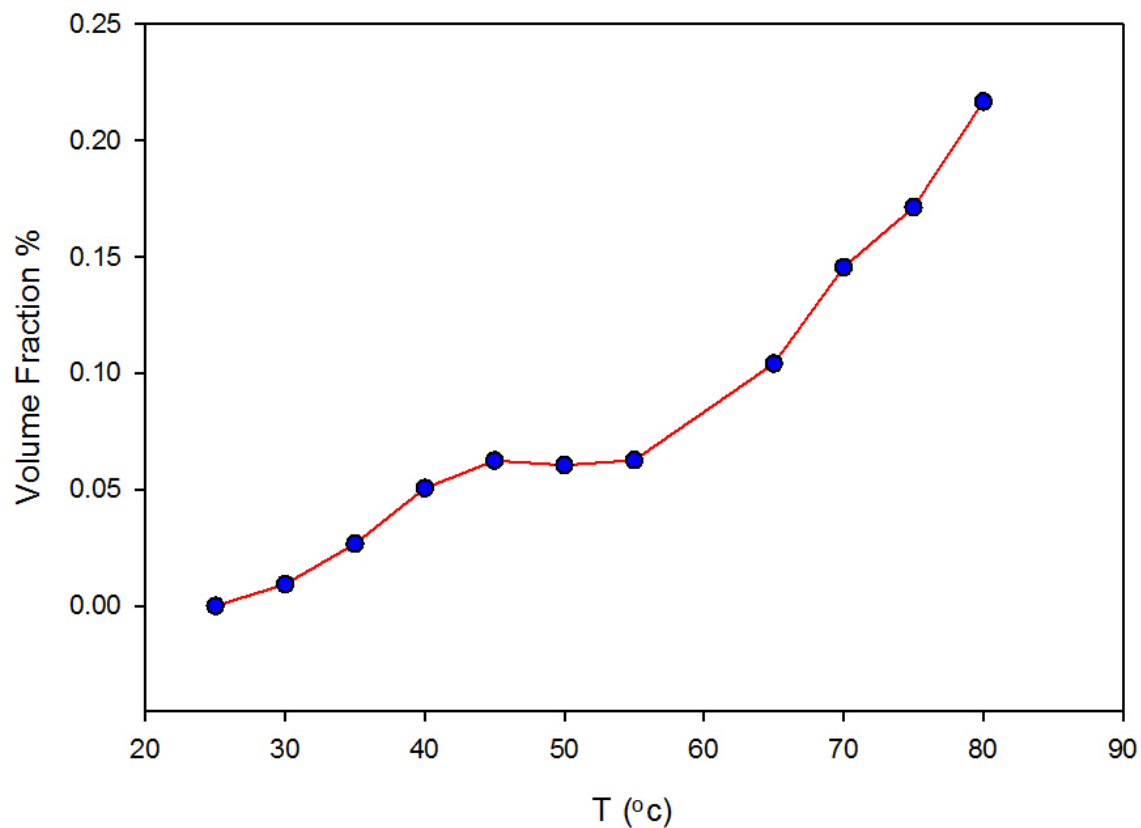


**Figure 5-24: Calculated volume fraction change due temperature for SP8888 in 3%wt NaCl based on the change in value of coating capacitance (Cc)**

### 5.2.2 Electrochemical Noise Testing (EN)

The measured noise currents and voltages were used to calculate the noise resistance using equation 5.1.

$$R_n = \frac{\sigma E}{\sigma I} \quad (5.1)$$

The calculated  $R_n$  values for SP2888 and SP8888 are reported in tables 5-4 and 5-5. At each temperature, six  $R_n$  values were calculated. These values showed large deviations (25-50%), which can be attributed to the noisy nature of  $E$  and  $I$  used in calculation. Then the averaged

value for each group was considered to represent the  $R_n$  of the coating at that temperature.  $R_n$  average values for both coatings at different temperatures are presented in figures 5-25 and 5-26.  $R_n$  decreased in good consistency with the results from the EIS method. At room temperature,  $R_n$  was in the range of 9 and 10 (on the log scale) for SP2888 and SP8888 respectively. Similar values were reported by Mills *et al.* for polyurethane coatings in recent work. However, this value started to decrease with a decreasing slope as the temperature was increased, but no abrupt change that may be linked to  $T_g$ . Figures 5-27 and 5-28 show that  $R_n$  follows a pattern similar to  $Z_{max}$ .

**Table 5-4:  $R_n$  ( $\Omega$ ) for SP2888 at temperature range of 20 to 80°C**

| No. T | 20       | 30       | 33       | 37       | 47       | 50       | 55       | 60       | 75       | 80       |
|-------|----------|----------|----------|----------|----------|----------|----------|----------|----------|----------|
| 1     | 2.12E+09 | 4.62E+08 | 1.94E+08 | 3.56E+07 | 2.32E+07 | 1.48E+07 | 7.42E+06 | 3.79E+06 | 6.44E+06 | 2.31E+06 |
| 2     | 1.20E+09 | 5.15E+08 | 1.01E+08 | 4.12E+07 | 1.09E+07 | 1.99E+07 | 2.07E+06 | 1.53E+07 | 3.30E+06 | 8.47E+06 |
| 3     | 2.12E+09 | 2.19E+08 | 1.15E+08 | 5.53E+07 | 1.64E+07 | 1.04E+07 | 9.49E+06 | 1.86E+06 | 6.27E+06 | 2.72E+06 |
| 4     | 1.25E+09 | 2.26E+08 | 8.33E+07 | 2.97E+07 | 1.86E+07 | 2.01E+07 | 5.72E+06 | 1.78E+07 | 5.89E+06 | 6.17E+06 |
| 5     | 1.28E+08 | 1.05E+08 | 8.62E+07 | 3.79E+07 | 1.29E+07 | 2.48E+07 | 8.98E+06 | 2.79E+06 | 5.18E+06 | 2.85E+06 |
| 6     | 1.35E+09 | 4.28E+08 | 4.13E+07 | 1.61E+07 | 2.53E+07 | 1.83E+07 | 3.60E+06 | 3.60E+06 | 7.69E+06 | 4.01E+06 |

**Table 5-5:  $R_n$  for SP8888 at temperature range of 20 to 90°C**

| No. T | 20       | 30       | 35       | 40       | 45       | 55       | 65       | 75       | 90      |
|-------|----------|----------|----------|----------|----------|----------|----------|----------|---------|
| 1     | 4.07E+09 | 1.2E+10  | 4.63E+08 | 1.76E+08 | 3.91E+08 | 1.77E+08 | 75982093 | 20464535 | 1356669 |
| 2     | 2.83E+09 | 4.49E+09 | 1.13E+08 | 71884049 | 2.41E+08 | 64564815 | 15384887 | 27320789 | 1841730 |
| 3     | 3.13E+09 | 36844624 | 1.77E+08 | 71884049 | 95298845 | 2E+08    | 26902232 | 14232247 | 2066866 |
| 4     | 1.02E+10 | 58404011 | 89355121 | 60778482 | 1.25E+08 | 28222138 | 16484186 | 25872056 | 3301925 |
| 5     | 6.89E+09 | 71372502 | 89355121 | 1.75E+08 | 5.96E+08 | 38767695 | 53604416 | 29058475 | 3883390 |
| 6     | 7.31E+09 | 52562834 | 44205175 | 1.32E+08 | 5.96E+08 | 4.29E+08 | 61196762 | 24982219 | 4796270 |

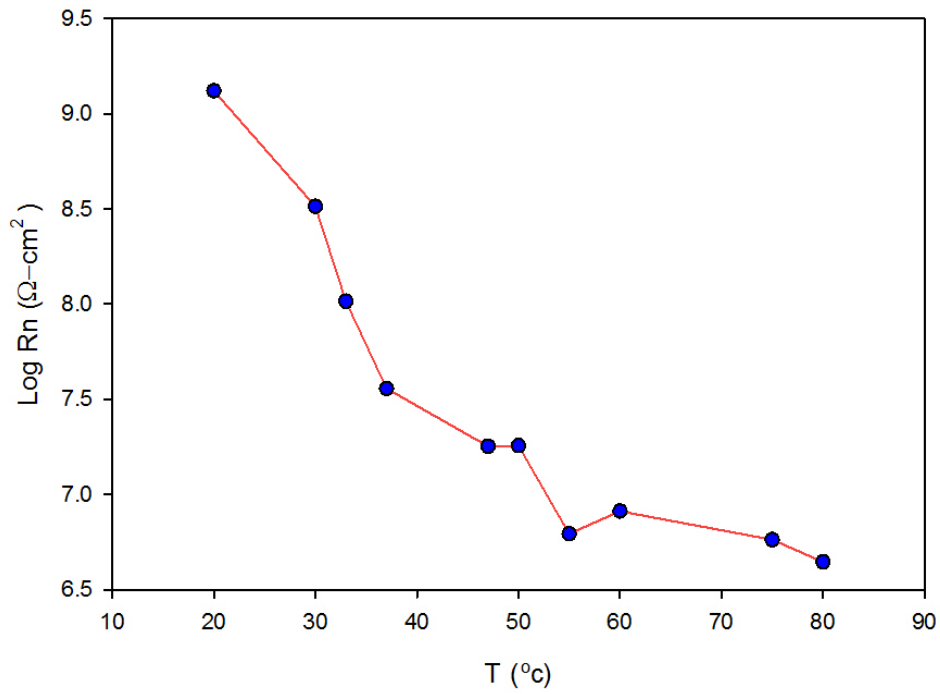


**Figure 5-25: Log Rn Vs T (°C) for SP2888 in 3%wt NaCl**

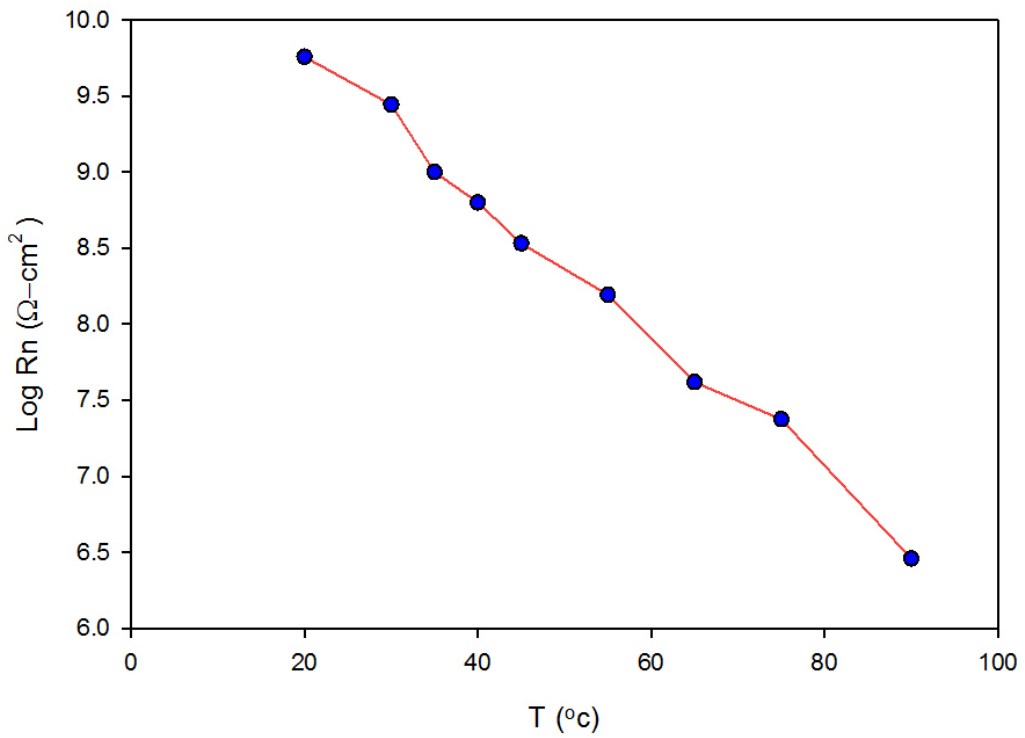


**Figure 5-26: Log Rn Vs T (°C) for SP8888 in 3%wt NaCl**

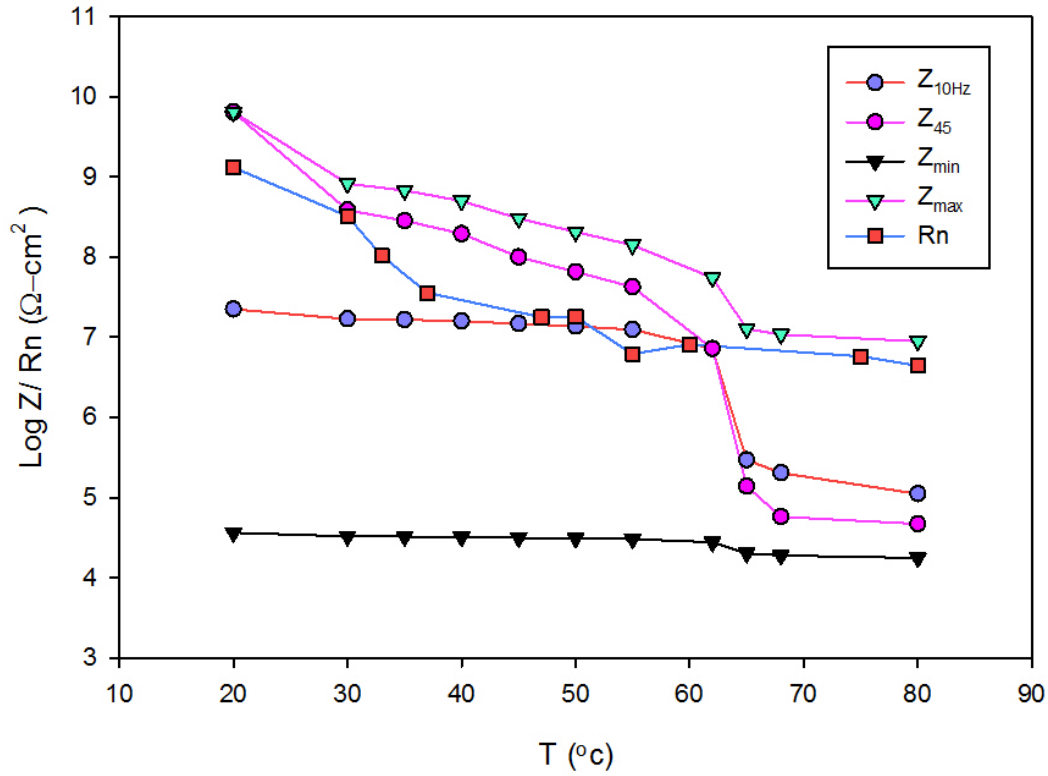


Figure 5-27: Impedance from EIS and Resistance from Rn ( $\Omega\text{-cm}^2$ ), for SP2888, vs T ( $^{\circ}\text{C}$ )

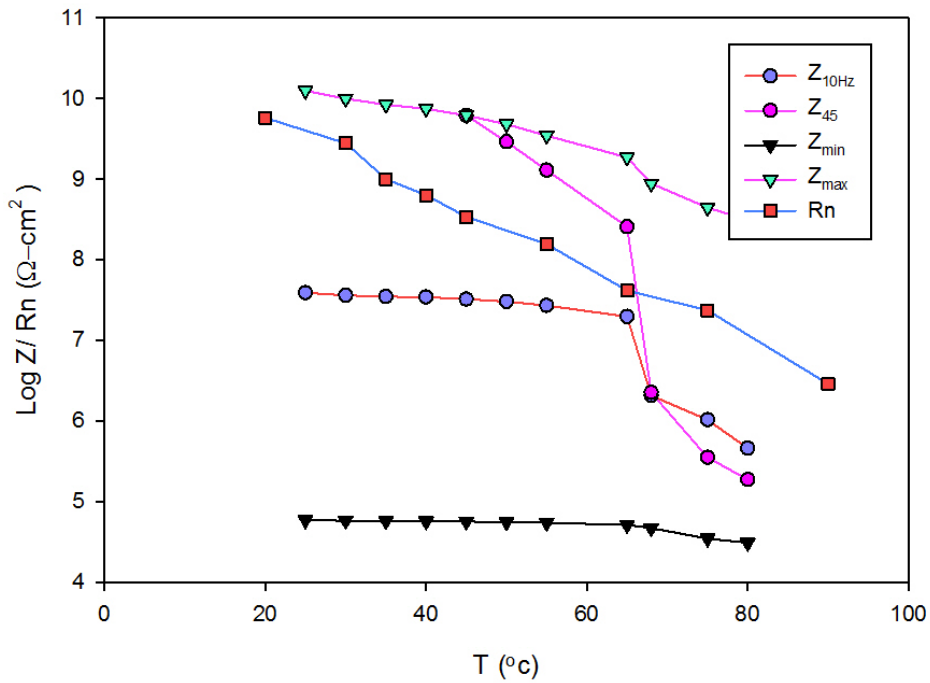


Figure 5-28: Impedance from EIS and Resistance from Rn ( $\Omega\text{-cm}^2$ ), for SP8888, vs T ( $^{\circ}\text{C}$ )

## 6 Summary and Conclusions

In this work, the main goal was to study the corrosion behavior of two coatings (SP2888 and SP8888) around their  $T_g$ 's in the existence of cathodic protection by applying a proper value of DC voltage in all tests using an EIS technique. Actually, characterization of the coatings was done first by utilizing various techniques. DSC was used to evaluate the  $T_g$ 's. Consequently, the testing temperature range for the experiment was set between 20 to 80°C, an EDX/SEM technique was used to study the morphology of the coatings and a gravimetric test was done to evaluate the weight fraction of the samples at different points in the temperature range of the test. Thereafter, EIS tests were performed on the carbon steel coated samples using a lab-made, three-electrode flat cell. In the cell, a graphite electrode was used as a counter electrode while the carbon steel of the sample was used as the working electrode and a saturated calomel electrode was used as a reference. A 3%wt sodium chloride was used as an electrolyte and the frequency range of testing was from  $10^{-2}$  to  $10^4$ . Additionally, electrochemical noise tests were performed on the samples to evaluate the effect of the temperature on the noise resistance in order to provide a second means of evaluation. The results from the characterization and electrochemical testing techniques were discussed and the following has been concluded:

- The measured  $T_g$  values for SP2888 and SP8888 using DSC were found to be 58.3°C and 63.7°C.
- The morphological analysis has shown that the average blister diameter for SP8888 was almost half of that of SP2888 which can be the reason for the higher water intake for SP2888 compared to SP8888, as shown in figure 5-8.

- At low temperature (20°C), the impedance was high (12 and 11.5 on a log scale) ( $\Omega\text{-cm}^2$ ) for both coatings. On the other hand, the phase for SP2888 was  $-45^\circ$  while the phase of SP8888 was about  $-60^\circ$ . As the temperature increased to 80°C, the impedance at low frequency for both coatings dropped drastically, to 9 and 10 (on the log scale) respectively, which was accompanied with a phase change from capacitive to resistive behavior.
- On the temperature domain,  $Z_{\theta=45}$  and  $Z_{f=10}$  were sensitive to the temperature changes,  $Z_{\theta=45}$  was the most sensitive. Also, they have showed abrupt changes around  $T_g$ 's unlike  $Z_{\min}$  and  $Z_{\max}$ .
- From the EEC of the coatings,  $R_{ct}$  was the most dominant resistive value in the system.  $R_{ct}$  gradually dropped as the temperature increased from 20°C to 80°C. Meanwhile, the error on this value increased after  $T_g$  (error ratio = 4 and 0.35 for SP2888 and SP8888 respectively), which indicates a drastic drop in the actual value of the coatings. CPE behaved in the same way with, the admittance (Y) drastically dropping above  $T_g$ . Most of the phase changes measured in EIS was contributed by CPE. On the other hand, the capacitance (Cc) slightly increased over the whole temperature change, as shown in tables 5-2 and 5-3. Eventually, the calculated volume fraction based on Cc values, was in agreement with gravimetric test results. Also, Cc and Rc have shown slope changes around  $T_g$  values.
- The developed EEC model was suitable to represent the coatings at temperatures below their  $T_g$ 's but at a higher temperature the model cannot be used to represent these coatings due the large value of Goodness of Fit, which indicates an occurrence of significant changes in the coatings.
- The calculated  $R_n$  values from EN tests were compatible with  $Z_{\max}$  values. It has shown a linear drop from 9.5 to 6.5 (on the log scale) for both coatings as the temperature increased.

## 7 Future work

- Similar work on other pipeline coatings is needed in order to build a general understanding of coating protection behavior around  $T_g$  in the existence of cathodic protection.
- EIS often uses water as an electrolyte for testing. Water is found to be not good enough for accurate testing due to the hydrophilic characteristic of water. Testing with  $D_2O$  will provide an opportunity to conduct more accurate tests
- Cathodic protection negatively charges the pipeline to shift it to the immune region. Failure of cathodic system will make the pipeline potential target for the corrosive species. Testing the same coating without cathodic protection will give a chance for evaluation in aggressive environments.
- More focus on studying charge transfer to understand its role on the corrosion protection behavior and how that can be influenced by  $T_g$ .

## 8 References

- Afantitis, A., Melagraki, G., Makridima, K., Alexandridis, A., Sarimveis, H., Iglessi-Markopoulou, O., 2005. Prediction of high weight polymers glass transition temperature using RBF neural networks. *J. Mol. Struct. THEOCHEM* 716, 193–198.
- Ahmad, Z., 2006a. Chapter 6 - Corrosion Control by Inhibition, in: Ahmad, Z. (Ed.), *Principles of Corrosion Engineering and Corrosion Control*. Butterworth-Heinemann, Oxford, pp. 352–381.
- Ahmad, Z., 2006b. Chapter 1 - Introduction to Corrosion, in: Ahmad, Z. (Ed.), *Principles of Corrosion Engineering and Corrosion Control*. Butterworth-Heinemann, Oxford, pp. 1–8.
- Akbarinezhad, E., Rezaei, F., Neshati, J., 2008. Evaluation of a high resistance paint coating with EIS measurements: Effect of high AC perturbations. *Prog. Org. Coat.* 61, 45–52.
- Angeles, M.E., Rodríguez, F., Magaña, C., 2012. Effect of heating on the performance of anticorrosive coatings. *Pigment Resin Technol.* 41, 42–48.
- Baldissera, A.F., Ferreira, C.A., 2012. Coatings based on electronic conducting polymers for corrosion protection of metals. *Prog. Org. Coat.* 75, 241–247.
- Beverkog, B., Puigdomenech, I., 1996. Revised Pourbaix diagrams for iron at 25–300 C. *Corros. Sci.* 38, 2121–2135.
- Bierwagen, G.P., Jeffcoate, C.S., Li, J., Balbyshev, S., Tallman, D.E., Mills, D.J., 1996. The use of electrochemical noise methods (ENM) to study thick, high impedance coatings. *Prog. Org. Coat.* 29, 21–29.
- Cantini, N.J., Mitton, D.B., Eliaz, N., Leisk, G., Wallace, S.L., Bellucci, F., Thompson, G.E., Latanision, R.M., 2000. In situ underfilm corrosion rate measurements by magnetic and electrochemical techniques. *Electrochem. Solid-State Lett.* 3, 275–278.
- Cao-Paz, A., Covelo, A., Farina, J., Novoa, X.R., Perez, C., Rodriguez-Pardo, L., Special Issue on The Sixth International Workshop on “Application of Electrochemical Techniques to Organic Coatings (AETOC)”, 2010. Ingress of water into organic coatings: Real-time monitoring of the capacitance and increase in mass. *Prog. Org. Coat.* 69, 150–157.
- Castela, A.S., Simoes, A.M., 2003. Assessment of water uptake in coil coatings by capacitance measurements. *Prog. Org. Coat.* 46, 55–61.
- Castela, A.S., Simoes, A M., 2003. Water sorption in freestanding PVC films by capacitance measurements. *Prog. Org. Coat.* 46, 130.
- Cheremisinoff, N.P., 1996. 2 - Design and corrosion, in: Cheremisinoff, N.P. (Ed.), *Materials Selection Deskbook*. William Andrew Publishing, Westwood, NJ, pp. 13–50.

- Corlett, N., Eiselstein, L.E., Budiansky, N., 2010. 2.03 - Crevice Corrosion, in: Cottis, B., Graham, M., Lindsay, R., Lyon, S., Richardson, T., Scantlebury, D., Stott, H. (Eds.), Shreir's Corrosion. Elsevier, Oxford, pp. 753–771.
- Cottis, R.A., 2006. Sources of electrochemical noise in corroding systems. *Russ. J. Electrochem.* 42, 497–505.
- Cottis, R.A., 2007. The significance of electrochemical noise measurements on asymmetric electrodes. *Electrochimica Acta* 52, 7585–7589.
- Curioni, M., Balaskas, A.C., Thompson, G.E., 2013. An alternative to the use of a zero resistance ammeter for electrochemical noise measurement: Theoretical analysis, experimental validation and evaluation of electrode asymmetry. *Corros. Sci.* 77, 281–291.
- Curioni, M., Cottis, R.A., Thompson, G.E., 2012. Interpretation of electrochemical noise generated by multiple electrodes. *Corrosion* 69, 158–166.
- Dong, C.F., Fu, A.Q., Li, X.G., Cheng, Y.F., 2008. Localized EIS characterization of corrosion of steel at coating defect under cathodic protection. *Electrochimica Acta* 54, 628–633.
- Dong Hwang, Y., Woon Cha, S., 2002. The relationship between gas absorption and the glass transition temperature in a batch microcellular foaming process. *Polym. Test.* 21, 269–275.
- Duarte, R.G., Castela, A.S., Ferreira, M.G.S., 2009. A new model for estimation of water uptake of an organic coating by EIS: The tortuosity pore model. *Prog. Org. Coat.* 65, 197–205.
- Feldstein, M.M., Kuptsov, S.A., Shandryuk, G.A., Platé, N.A., 2001. Relation of glass transition temperature to the hydrogen-bonding degree and energy in poly (N-vinyl pyrrolidone) blends with hydroxyl-containing plasticizers. Part 2. Effects of poly (ethylene glycol) chain length. *Polymer* 42, 981–990.
- Fu, A.Q., Cheng, Y.F., 2011. Characterization of the permeability of a high performance composite coating to cathodic protection and its implications on pipeline integrity. *Prog. Org. Coat.* 72, 423–428.
- Giacomelli Penon, M., Picken, S.J., Wübbenhorst, M., van Turnhout, J., 2007. Vapor diffusion in porous/nonporous polymer coatings by dielectric sorption analysis. *J. Appl. Polym. Sci.* 105, 1471–1479.
- Gracia-Fernández, C.A., Gómez-Barreiro, S., López-Beceiro, J., Tarrío Saavedra, J., Naya, S., Artiaga, R., 2010. Comparative study of the dynamic glass transition temperature by DMA and TMDSC. *Polym. Test.* 29, 1002–1006.
- Guermaz, N., Elleuch, K., Ayedi, H.F., 2009. The effect of time and aging temperature on structural and mechanical properties of pipeline coating. *Mater. Des.* 30, 2006–2010.

- Hasanov, R., Bilgiç, S., 2009. Monolayer and bilayer conducting polymer coatings for corrosion protection of steel in 1M H<sub>2</sub>SO<sub>4</sub> solution. *Prog. Org. Coat.* 64, 435–445.
- Hinderliter, B.R., Croll, S.G., 2009. Simulation of transient electrochemical impedance spectroscopy due to water uptake or oxide growth. *Electrochimica Acta* 54, 5344–5352.
- Hubbard, A., 2008. *Corrosion and Corrosion Control: An Introduction to Corrosion Science and Engineering*, fourth ed., R. Winston Revie, Herbert H. Uhlig (Eds.). John Wiley & Sons, Hoboken, NJ (2008). *J. Colloid Interface Sci.* 328, 463.
- Ibrahim, S.Y., 2005. Cathodic Protection System for Crude Oil Storage Tanks and Water Pipelines in the Refinery. *Pet. Sci. Technol.* 23, 601–609.
- Kendig, M., Hon, M., Warren, L., 2003. “Smart” corrosion inhibiting coatings. *Prog. Org. Coat.* 47, 183–189.
- Kim, S.H., Chung, J.W., Kang, T.J., Kwak, S.-Y., Suzuki, T., 2007. Determination of the glass transition temperature of polymer/layered silicate nanocomposites from positron annihilation lifetime measurements. *Polymer* 48, 4271–4277.
- Le Pen, C., Lacabanne, C., Pébère, N., 2000. Structure of waterborne coatings by electrochemical impedance spectroscopy and a thermostimulated current method: influence of fillers. *Prog. Org. Coat.* 39, 167–175.
- Le Thu, Q., Takenouti, H., Touzain, S., 2006. EIS characterization of thick flawed organic coatings aged under cathodic protection in seawater. *Electrochimica Acta* 51, 2491–2502.
- Leng, A., Streckel, H., Stratmann, M., 1998. The delamination of polymeric coatings from steel. Part 1: Calibration of the Kelvinprobe and basic delamination mechanism. *Corros. Sci.* 41, 547–578.
- Li, J., Jeffcoate, C.S., Bierwagen, G.P., Mills, D.J., Tallman, D.E., 1998. Thermal transition effects and electrochemical properties in organic coatings: Part 1-Initial studies on corrosion protective organic coatings. *Corrosion* 54, 763–771.
- Liu, A., Wang, X., Wang, L., Wang, H., Wang, H., 2007. Prediction of dielectric constants and glass transition temperatures of polymers by quantitative structure property relationships. *Eur. Polym. J.* 43, 989–995.
- Lowe, A.M., Eren, H., Bailey, S.I., 2003. Electrochemical noise analysis: detection of electrode asymmetry. *Corros. Sci.* 45, 941–955.
- Macdonald, J.R., Barsoukov, E., 2005. *Impedance spectroscopy: theory, experiment, and applications*. History 1, 8.

- Mills, D., Picton, P., Mularczyk, L., n.d. Developments in the electrochemical noise method (ENM) to make it more practical for assessment of anti-corrosive coatings. *Electrochimica Acta*. doi:10.1016/j.electacta.2013.09.067
- Nguyen, V.N., Perrin, F. X., Vernet, J. L., 2005. Water permeability of organic/inorganic hybrid coatings prepared by sol-gel method: a comparison between gravimetric and capacitance measurements and evaluation of non-Fickian sorption models. *Corros. Sci.* 47, 397–412.
- Nwankire, C.E., Dowling, D.P., 2010. Influence of nm-thick atmospheric plasma deposited coatings on the adhesion of silicone elastomer to stainless steel. *J. Adhes. Sci. Technol.* 24, 1291–1302.
- Oliveira, C.G., Ferreira, M.G.S., 2003. Ranking high-quality paint systems using EIS. Part I: intact coatings. *Corros. Sci.* 45, 123–138.
- Peng, Y.X., Zheng, Z.H., Ding, X.B., Zhang, W.C., Ye, Z.H., 2003. Nanometer polymer latex dispersion and its application in water-based coating. *Prog. Org. Coat.* 48, 161–163.
- Perera, D.Y., 2002. Effect of thermal and hygroscopic history on physical ageing of organic coatings. *Prog. Org. Coat.* 44, 55–62.
- Philippe, L., Sammon, C., Lyon, S.B., Yarwood, J., 2004. An FTIR/ATR in situ study of sorption and transport in corrosion protective organic coatings: Paper 2. The effects of temperature and isotopic dilution. *Prog. Org. Coat.* 49, 315–323.
- Rezaei, F., Sharif, F., Sarabi, A.A., Kasiriha, S.M., Rahmanian, M., Akbarinezhad, E., 2010a. Experimental evaluation of high solid polyurethane coating in the presence of salt at high temperature. *Mater. Corros.* 61, 681–688.
- Rezaei, F., Sharif, F., Sarabi, A.A., Kasiriha, S.M., Rahmanian, M., Akbarinezhad, E., 2010b. Evaluating water transport through high solid polyurethane coating using the EIS method. *J. Coat. Technol. Res.* 7, 209–217.
- Righetti, M.C., Ajroldi, G., Pezzin, G., 1992. The glass transition temperature of polymer-diluent systems. *Polymer* 33, 4779–4785.
- Rouw, A.C., 1997. Model epoxy powder coatings and their adhesion to steel. *Prog. Org. Coat.* 34, 181–192.
- Safuadi, M., Ridha, M., Huzni, S., Fonna, S., Ariffin, A.K., Daud, A.R., 2011. Optimization of Cathodic Protection System Design for Pipe-Lines Structure with Ribbon Sacrificial Anode Using BEM and GA. *Key Eng. Mater.* 462, 1267–1272.
- Seong, J., Frankel, G.S., 2012. Assessment of Coating Adhesion Degradation by Atomic Force Microscopy Scratching. *Corros. J. Sci. Eng.* 68, 032501–1.

- Shreepathi, S., Naik, S.M., Vattipalli, M.R., 2012. Water transportation through organic coatings: correlation between electrochemical impedance measurements, gravimetry, and water vapor permeability. *J. Coat. Technol. Res.* 9, 411–422.
- Shreir, L.L., 2010. 1.05 - Basic Concepts of Corrosion, in: Cottis, B., Graham, M., Lindsay, R., Lyon, S., Richardson, T., Scantlebury, D., Stott, H. (Eds.), *Shreir's Corrosion*. Elsevier, Oxford, pp. 89–100.
- Song, F.M., 2012. Predicting the chemistry, corrosion potential and corrosion rate in a crevice formed between substrate steel and a disbonded permeable coating with a mouth. *Corros. Sci.* 55, 107–115.
- Stafford, O.A., Hinderliter, B.R., Croll, S.G., 2006. Electrochemical impedance spectroscopy response of water uptake in organic coatings by finite element methods. *Electrochimica Acta* 52, 1339–1348.
- Szociński, M., Darowicki, K., Schaefer, K., 2010. Identification and localization of organic coating degradation onset by impedance imaging. *Polym. Degrad. Stab.* 95, 960–964.
- Talbot, J.D.R., 2008. Principles of corrosion engineering and corrosion control, Zaki Ahmed. Butterworths-Heinemann/ICChemE (2006). *Mater. Charact.* 59, 660–661.
- Tüken, T., Yazıcı, B., Erbil, M., 2006. The corrosion behaviour of polypyrrole coating synthesized in phenylphosphonic acid solution. *Appl. Surf. Sci.* 252, 2311–2318.
- Verkholantsev, V.V., 1995. Heterophase and self-stratifying polymer coatings. *Prog. Org. Coat.* 26, 31–52.
- Xia, D., Song, S., Wang, J., Bi, H., Han, Z., 2012. Fast evaluation of degradation degree of organic coatings by analyzing electrochemical impedance spectroscopy data. *Trans. Tianjin Univ.* 18, 15–20.
- Yang, B., Min Huang, W., Li, C., Hoe Chor, J., 2005. Effects of moisture on the glass transition temperature of polyurethane shape memory polymer filled with nano-carbon powder. *Eur. Polym. J.* 41, 1123–1128.
- Zarras, P., Anderson, N., Webber, C., Irvin, D.J., Irvin, J.A., Guenther, A., Stenger-Smith, J.D., 2003. Progress in using conductive polymers as corrosion-inhibiting coatings. *Radiat. Phys. Chem.* 68, 387–394.
- Zuo, Y., Pang, R., Li, W., Xiong, J.P., Tang, Y.M., 2008. The evaluation of coating performance by the variations of phase angles in middle and high frequency domains of EIS. *Corros. Sci.* 50, 3322–3328.